UNIVERSITY
OF LATVIA

Summary
of Doctoral Thesis

Kirils Surovovs

NUMERICAL MODELLING OF LARGE DIAMETER SILICON CRYSTAL GROWTH WITH PEDESTAL PROCESSS

Riga 2023

UNIVERSITY OF LATVIA

FACULTY OF PHYSICS, MATHEMATICS AND OPTOMETRY

Kirils Surovovs

NUMERICAL MODELLING OF LARGE DIAMETER SILICON CRYSTAL GROWTH WITH PEDESTAL PROCESS

Summary of Doctoral Thesis

Submitted for the Doctoral Degree (Ph.D.) in Physics
Subfield: Fluid Mechanics

Riga, 2023

The doctoral thesis was carried out at the Faculty of Physics, Mathematics and Optometry, Institute of Numerical Modelling, University of Latvia, from 2015 to 2023.

This summary contains an introduction, 2 chapters, conclusions and a reference list.

Form of the thesis: the collection of research papers in physics, subfield of fluid mechanics.

Thesis supervisor: Dr. phys. **Jānis Virbulis**

Thesis reviewers:

1. Dr. phys. **Imants Kaldre**, leading researcher in the Institute of Physics, University of Latvia
2. Dr. phys. **Wolfram Miller**, leading researcher in the Berlin Institute for Crystal Growth, Germany
3. Dr. phys. **Gundars Ratnieks**, process developer at Siltronic AG, Germany

The thesis will be defended at the public session of the Doctoral Committee of physics, University of Latvia, on 2 June 2023 at 15:00 in Riga, Jelgavas street 3. The thesis is available at the Library of the University of Latvia, Kalpaka blvd. 4.

The author of the thesis participated in the project "Strengthening the capacity of the UL PhD programme in the new doctoral model" – University of Latvia, Id. Nr. 8.2.2.0/20/I/006.

Doctoral Committee of physics, University of Latvia

chairman: _____ /Dr. phys. **Andris Jakovičs**/

secretary: _____ /**Sintija Siliņa**/

ISBN 978-9934-36-003-9

ISBN 978-9934-36-004-6 (PDF)

Annotation

The present work is devoted to the numerical modelling of silicon crystal growth with pedestal process – a cost-effective alternative to floating zone process. In the considered version of the pedestal process, heating is realized with high-frequency inductor (on top of the pedestal) and middle-frequency inductor (around the side surface of the pedestal). The present work describes modelling of heat transfer and phase boundaries in axially symmetrical approximation, neglecting the melt flow in most cases. For the case with small crystal diameter (seed crystal), the melt flow is modelled and its influence on melting interface shape is analyzed. The shape of high-frequency inductor was optimized, using the algorithm of gradient descent. The distance between the centers of melting and crystallization interfaces was used as a target function to prevent melt center freezing. For crystal diameter of 100 mm, the optimal high-frequency inductor shape was obtained and an algorithm of the change of heating power during the cone phase was proposed.

Keywords: silicon, crystal growth, pedestal method, numerical modelling.

Table of Contents

List of abbreviations and variables

Si	silicon
FZ	floating zone [method]
HF	high-frequency
MF	middle-frequency
PM	pedestal method
EM	electromagnetic
CZ	Czochralski
ETP	external triple point
ITP	internal triple point
PID	proportional-integral-derivative [control]
FS	free surface
HD	hydrodynamics
H_M	melt height
D_C, R_C	crystal diameter, radius
D_P, R_P	pedestal diameter, radius
H_P	pedestal height
H_Q	heating region height
z_Q	distance from the heating region to ETP
f_t	target function
α_{ETP}	the angle between the free surface and the vertical at ETP
$z_{\max}$	zone height
R_{ind}	internal radius of the inductor
H_{ind}	inductor height above the pedestal rim
r, z	radial and vertical coordinates
T	temperature
$\vec{v}$	velocity
q	heat flux density
Q	integral heat flux
I	inductor current
f	inductor frequency
	inductor slice parameters (see. Fig. 2.3):
r_{ind}, z_{ind}	radial and vertical coordinates
c_{ind}	curvature radius
k_{ind}	length
α_{ind}	inclination angle

1 Introduction

Man had admired crystals for long,
as he had appreciated their beauty
B. Subashini and M. Geetha

1.1 Preface

For the modern semiconductor device industry, silicon crystals are virtually irreplaceable. Due to very large – up to several billion dollars [1] in 2020 – global market size, even minor improvements in silicon production process are receiving researchers' attention.

The importance of numerical modelling

Crystal growth experiments, that are used for the development of growth equipment, are rather costly and technically challenging. The experimental results are of limited quality and sometimes are not even able to give insight into all principal features of the growth process. For example, the shape of the crystallization interface can be experimentally determined by lateral photovoltage scanning method [2]. One of the numerous examples of this method in Si crystal characterization is the study from A. Lüdge et. al. [3]. It gives a valuable insight into the crystal rotation influence on the crystallization interface shape (see Fig. 1.1), and the evolution of the interface shape in time can be traced. However, this experiment does not show, and is unable to show, the changes in temperature gradients, shape of the free surface, melt flow, and other aspects that lead to the depicted result. To fully understand the demonstrated effect and employ it for process development, comprehension of temperature field *inside* the molten zone is necessary.

To get this kind of insight into crystal growth processes, numerical modeling is widely used. It allows not only to reduce the number of expensive experiments, but also to supplement existing experiments by describing process features that are very hard to measure. Examples include distributions of physical fields inside solid, melt and surrounding

atmosphere: temperature, velocity, electromagnetic field, dopant concentration, thermal stresses etc.

Numerical modelling is customarily used for the development of industrial purposes, even for minor improvements of crystal growth equipment. It is therefore utterly necessary to use numerical modelling for the development of a novel industrial process. The present work describes **numerical modeling of silicon crystal growth with pedestal method**, with a focus on making the growth of **large diameter crystals** possible.

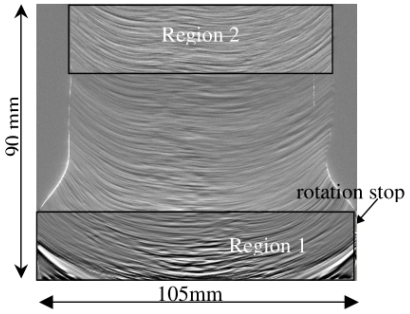

Figure 1.1. Lateral photovoltage scanning measurement of the axial cut of the grown crystal [3]. Region 1 corresponds to the process stage with crystal rotation rate of 5 rpm, region 2 – the process stage without rotation.

Brief overview of crystal growth methods

Depending on the used material and intended applications, different crystal growth methods are used. All existing methods can be roughly classified in four categories [4], which are described in the subsections below, along with comments on their applicability for silicon single crystals.

Solid growth

The solid-state growth method is based on atomic diffusion, which is usually very slow. Examples of these methods are annealing, heat treatment, polymorphic phase transitions, etc., which are mainly used in metallurgical processes. Recently some of these methods, such as grain boundary migration, have been investigated for single crystals with complex chemical composition or incongruent melting behavior [5]. Anyway, the solid-state growth techniques are not considered for silicon single crystals, because

other techniques are simpler, faster and more well-established, as it will be shown further.

Solution growth

This is the oldest and probably the most well-known category of growth methods – crystallization of ionic salts, like NaCl, from aqueous solutions is even sometimes used in primary schools. Its advantages are simplicity of equipment and high degree of crystal perfection (the crystals grow at temperatures well below their melting point). However, the methods from this category are ill-suited for silicon: it does not dissolve in water and requires unusual solvents [6].

From vapor phase

The growth from vapor, where the atoms or molecules of substance are introduced into the reactor by a suitable carrier gas, is now widely used to grow thin films and epitaxial (i.e., specifically oriented with respect to substrate) layers. These techniques primarily involves three stages: vaporization, transport, and deposition. In the case of silicon, however, chemical vapor deposition is used mainly to [7]:

- grow thin silicon films,
- obtain the high-purity polycrystalline, which then needs to be remelted and regrown into single crystals.

The chemical vapor deposition is the main method for the production of semiconductor grade polycrystalline Si [8], yet the deposition of single crystals is not cost-effective due to long process times [9]. The usage of very toxic compounds [10] – mainly trichlorosilane $SiHCl_3$ and silane SiH_4 – may be considered as another drawback of growth from vapor [11].

From melt

More than half of the crystals that are used in technology are grown from melt [4]. This technique requires that the material melts without decomposition, exhibits low chemical activity and has relatively low vapor pressure. Silicon fulfills those requirements [12]. There are several methods, how crystals can be grown from melt:

- **Bridgman** – the material is melted in a closed container, and then is cooled by slowly moving the container from high-temperature zone

(usually the top part of the furnace) to low-temperature zone (bottom part) [13]. A variation of this technique that uses elongated open container with short walls is known as Horizontal Direct Crystallization or the Bagdasarov method [14].

- **Directional solidification** – another modification of the Bridgman method, where the container and furnace system is held stationary, and the temperature change is ensured by a multiple-zone furnace system [15].

- **Czochralski** – polycrystalline material is melted in a crucible, a seed crystal is introduced in the center of the free surface, and then pulled upwards from the melt. This technique helped to grow dislocation-free[1] silicon crystal in 1958 [16], and now it is the main method for commercial Si single crystal growth due to its high speed and low cost [17].

- **Granulate crucible** – the method is similar to the Czochralski method, except that in the beginning of the process the quartz crucible is filled with Si granules, and the heating is applied from above. It ensures that a part of the granulate is not molten and separates liquid Si from crucible walls [18]. Heating is realized with high-frequency inductor, thus graphite heaters are avoided and lower content of impurities is reached [19].

- **Floating zone** – the method is crucible-free, i.e. molten material does not touch other system parts, and the molten zone "floats" between the feed rod (supplied from above the melt) and grown single crystal (located below the melt). Heating can be provided by high-frequency inductor or by optical devices [20]. First applications of this method were realized for Si in 1953 [21], when the crystal with diameter of 5 mm was grown. Since then the maximal possible crystal diameter has been increased 40-fold [22]. This method is the second most widely used single crystal growth method for silicon [17].

- **Pedestal** – this method is similar to the floating zone method, only with the feed rod located at the bottom and the crystal pulled from the top [23]. The method will be described in more details in the next subsection.

[1] A dislocation is a linear defect in the crystal lattice, i.e., a line where periodical structure abruptly changes.

Crucible-free crystal growth from melt

Some of the existing crystal growth methods (e.g. Czochralski method or directional solidification method) require a crucible to hold the molten material. However, there are applications for which quality requirements are so high and allowable impurity content is so low that crucible-free methods should be used. Some examples of such applications for Si single crystals are high-power semiconductor devices and detectors. Another application is remelting of a part of polycrystalline Si rod and recrystallizing it in form of single crystal, for its characterization by Fourier-transform infrared (FTIR) spectroscopy [24].

Probably the most well-known crucible-free crystal growth method is the floating zone (FZ) method, where melting is realized by high-frequency (HF) electromagnetic (EM) one-turn inductor. In FZ method, the feed rod is located above the inductor, and melting occurs at the bottom part of feed rod (see Fig. 1.2(a) and Fig. 1.3(a)). This boundary – open melting front – where feed material is melting and flowing downwards, requires high feed rod quality and complicates the control of the growth process. This increases the costs of feed rod preparation.

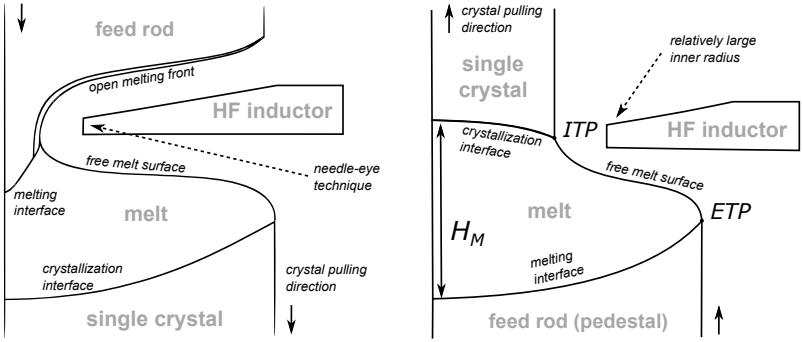

(a) Floating zone method **(b)** Pedestal method

Figure 1.2. Axially symmetrical sketches of the floating zone method and the pedestal method.

Another option is to use a recently proposed method of growth from the granulate crucible. An advantage of this method, in comparison to FZ, is bypassing of time-consuming and expensive production of feed rod [26], because the granulate can be manufactured directly from trichlorosilane [27]. However, this method is novel and thus has not been widely adopted yet

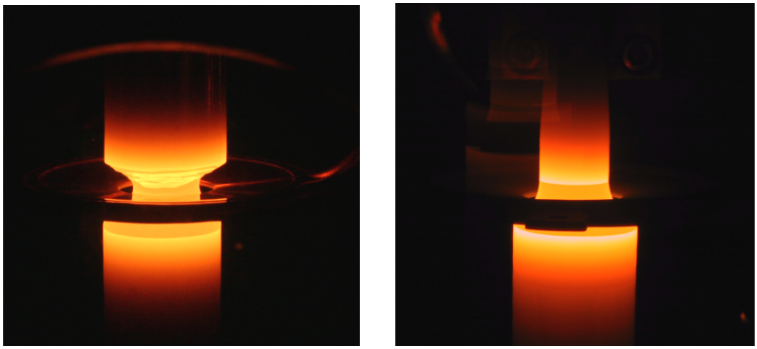

(a) Floating zone method **(b)** Pedestal method

Figure 1.3. Photographs of crystal growth processes, M. Wünscher et. al. [25].

due to lack of experience.

The pedestal method (PM), firstly proposed by Dash [23], is a simpler alternative to FZ method. It lacks such complicated feature as open melting front, because the molten Si resides at the top surface of the feed rod (pedestal), see Fig. 1.2(b). Therefore, process control can be simpler, and feed rod requirements can be lower in PM, than in FZ.

However, PM has a limitation on inductor shape: "needle-eye" inductors (with inner diameter that is smaller than the single crystal diameter, see Fig. 1.2(a)) that are used in FZ method cannot be used in PM. In combination with 11° meniscus angle requirement [28], it leads to a risk of melt center freezing, because inductor is far from the center of the melt. Complications may arise also during the melting of pedestal upper surface at the beginning of the process (see more information in Section 3.3.1).

Technological context of the pedestal method

It was proposed in a patent from 1988 that the cost issues of feed rod production for FZ process could be solved by using feed rods grown by Czochralski (CZ) method [29]. Nevertheless, HF induction heating problems (e.g. generator construction or high chamber pressure for the prevention of arching due to high voltage) and high feed rod requirements (the necessity of low oxygen content that is hard to ensure in CZ) still remain [30]. Therefore, even while CZ method allows to grow high-quality feed rods with diameters up to 300 mm, the information about FZ crystals that exceed 200 mm diameter is still absent.

These circumstances motivate to investigate the applicability of PM for Si single crystal growth. Pedestal can be heated not only by HF (1–3 MHz) inductor, but also additional heating by electron beam or middle-frequency inductor [31] can be used to avoid multiple problems like electrical breakdown near the main HF inductor and generator construction issues [32]. Another benefit of PM is the possibility of pill-doping through axial holes in the pedestal. Due to larger (in comparison to FZ) melt volume, the melt in PM can store more doping material and thus ensure more homogeneous axial distribution of dopant atoms [33].

PM is especially promising in the light of the availability of large diameter high-purity polycrystalline silicon rods [34]. This condition is fulfilled in *KEPP EU* company [34, 35], where these rods are obtained with the method similar to Czochralski method: the growth from a melt located in its own skull (solidified layer of Si on the crucible walls) using electron beam heating [36]. The electron beam heating allows to achieve lower energy consumption and lower impurity content [30] in comparison to CZ method [37], thanks to the intensive use of numerical modelling for the optimization of electron gun [38].

1.2 Motivation

As shown in the subsection above, the pedestal method can be considered as an alternative to the floating zone method. In some aspects, the pedestal method is simpler than the floating zone method – e.g., in process control, raw material requirements. As the *KEPP EU* factory produces large diameter polycrystalline rods (diameters up to 300 mm), the implementation of PM in the same factory can be a significant technological advantage.

However, large diameter silicon single crystals have not yet been grown by the pedestal method (see literature review below), therefore numerical modelling is needed to develop this growth process. This is one of the reasons why this thesis is important in the context of industrial silicon crystal growth in Latvia.

The Semiconductor Technology Laboratory, which is a part of the Institute of Numerical Modelling, University of Latvia, has accumulated extensive experience in Si crystal growth simulations by modelling FZ and CZ processes. The existing developments and the experience of the Institute's staff facilitate the creation of the PM numerical model, thus

improving the chances of achieving the goal of this thesis.

1.3 Literature review

The brief overview of crystal growth methods is provided in Sec. 1.1. This section, in turn, describes the pedestal method in more details and presents the overview of the development of numerical modelling for crucible-free Si crystal growth.

Pedestal method

The first mention of PM for silicon crystal growth is found in 1958, in the paper from William C. Dash [23]. He demonstrated a possibility of growing crystals with diameters about 12 mm from the pedestal with similar diameter. The pedestal was slotted, because its increased surface area simplifies its melting by HF coil. He also showed that dislocation-free crystals can be grown: if the growth begins with high pulling speed, and crystal diameter is small at the beginning of the process, then dislocations propagate to the surface and are eliminated [39][2]. A change of pedestal shape from cylindrical to conical allowed Dash to improve the process stability and to grow longer crystals of diameter 12 mm (Si) or 6 mm (Ge) [40].

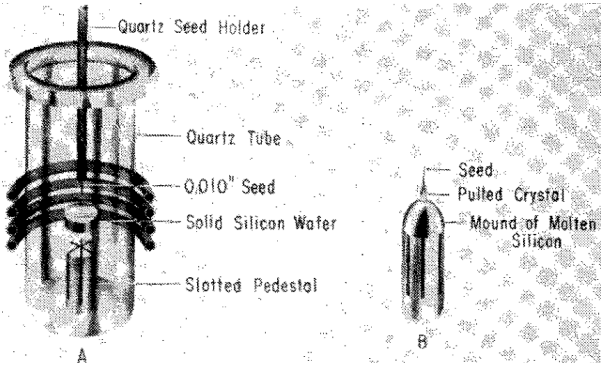

Figure 1.4. The scheme of the pedestal method (A) and melt shape during the growth process (B). The illustration from the Dash's article, that mentions the pedestal method for the first time in scientific literature [23].

[2]Rather surprisingly, the so-called "Dash neck" method, which is now very widely used in CZ crystal growth, was first published for the pedestal method!

Pedestal-grown silicon crystals, that were since then reported in literature, are very small by the modern market standards. For example, historical use of PM includes 4–5 mm for investigations with x-ray topography [41] and 9 mm diameter [42] for silicon bicrystals (grown from a seed with a grain boundary), as well as for substrates for chemical vapor deposition [43]. And even smaller diameters – below 2 mm – are sometimes used in Si crystal growth for photovoltaics [44]. The reports of such small sizes may be explained by the fact that PM is more convenient for crucible-free growth of small crystals in comparison to FZ: the upper part of the feed rod is easier to melt, and then to touch by a small seed crystal, than the bottom part.

According to von Ammon et. al., in PM crystal diameter can reach only 20 mm, because maintaining the zone shape is difficult [45]. Riemann et. al. also reported growing 15–20 mm crystals [33]. However, there is a modification of PM by T. F. Ciszek that employs heating with electron beam, and this modification allowed to reach diameters up to 40 mm [46], growing form 100 mm pedestal. The electron beam impact zone was fixed relative to the crystal. An important feature of Ciszek's approach was the eccentric position of the grown crystal – its axis was shifted from the pedestal axis by 20 mm. In the eccentric setup, the pedestal was moving through the electron beam impact zone during the rotation, and thus exposing the whole upper surface; unlike the axially symmetric setup, where the electron beam impact zone did not reach outer parts of the pedestal. Therefore, the eccentric configuration allowed to heat the pedestal more homogeneously.

Due to aforementioned limitations of crystal diameter, FZ process was characterized by W. Zulehner and D. Huber as the "only serious competitor to Czochralski crystal pulling" [47], while PM was mentioned only for small crystal production, e.g. for seed crystals. Despite such modest description of PM, the goal of the present work is to demonstrate the possibility of large crystal growth from pedestal. In order to achieve this goal, numerical modelling is very useful.

Numerical modelling of crucible-free Si crystal growth

Mathematical modelling has been used to improve and develop different crucible-free crystal growth methods since at least 1970s. For example, molten zone shape in FZ was modelled numerically by Coriell and Cordes [48], who neglected the influence of melt flow. However, the devel-

opment of models was very rapid, and already in 1978 convection patterns in FZ melt were analyzed [49], then the simulations of Marangoni force [50] and EM force [51] influence were also performed. All these effects (melt convection, Marangoni force, EM force) were coupled with simulations of molten zone shape in 1995, and the unsteady velocity oscillations were described [52]. Following the increase of computers' capabilities, the introduction of 3D models (instead of previously used axially symmetric ones) for EM field was made in early 1990s [53], and for the melt flow – in 2000 [54].

All aforementioned research regarded FZ method, as it is the most popular method of crucible-free Si crystal growth. However, there are studies that demonstrate the usefulness of numerical modelling for other methods as well. For example, the development of silicon growth from granulate crucible (the method itself has been patented in 2011 [18]) was intensively supported by numerical modelling. Simulation results had been published even before the first experimental results:

- Axially symmetrical model of EM field and silicon temperature was for the first time described in 2014 [55].
- The model was improved by comparison between different solvers, supplemented by 3D geometry and validated by comparison with simple cases (analytical solution, experimentally measured magnetic field generated by an inductor without load) in 2017 [56].
- The growth of crystals with diameter of 60 mm was reported and the image of experimental apparatus was published in 2018 [57].
- Impurities and defects were studied in a grown 60 mm crystal in 2020 [19]. In the same year, a model of process control has been developed and experiments conducted to determine unknown model parameters [58].

Numerical modelling of the pedestal method

In contrast with FZ and granulate crucible methods, there are virtually no mentions of the numerical modelling of PM for silicon in scientific literature. The only exception is a short mention of *FEMAG/FZ* software [59] potential to model PM, which was tested with a proof-of-concept simulation and without any input from the experimental system, see Fig. 1.5. In this example, molten zone height and free surface shape are imposed as simulation input parameter rather than calculated.

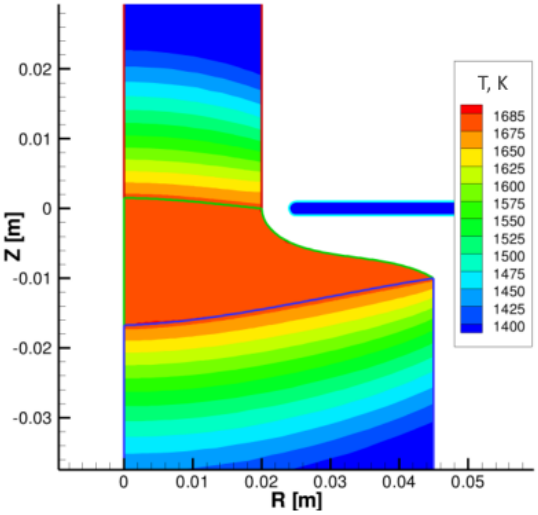

Figure 1.5. A proof-of-concept calculations of pedestal method: temperature field in silicon, obtained with *FEMAG/FZ* software [25].

Moreover, if laser-heating pedestal growth (which is mainly suited for thin oxide fibers with diameters less than 1 mm [60]) is not considered, there are no publications about the modelling of PM for *any material*, except the article by M. Wünscher et. al, which describes the modelling of germanium crystal pulling [61]. The article shows that *FEMAG/FZ* software was adapted for PM, thus the coordinates of the free surface are not calculated, but measured from an experiment photograph and passed as a simulation input.

Despite the long time since the invention of PM, its numerical models are hardly described in the scientific literature. This can be explained by the relatively low popularity of PM compared to FZ and CZ methods, especially in the case of silicon crystal growth. Since the FZ method has been invented earlier and also allows the use of an inductor with a small inner diameter (i.e. smaller than the diameter of the grown crystal), it has developed faster and now is more relevant than PM for industrial processes. Consequently, another aspect that makes the modelling of PM difficult is the lack of experimental data. Therefore, the pedestal method almost has not gotten any attention of numerical modellers so far.

1.4 Novelty of the thesis and author's contribution

From the previous subsection it can be concluded that the phase boundary calculations included in this thesis are essentially the first simulations of their kind: silicon growth by the pedestal method is numerically modelled for the first time. For the first time, the shape of the free surface in a pedestal system is calculated numerically rather than provided as input data. The melt flow simulations and the high-frequency inductor optimization calculations are also novel: studies of this kind for pedestal systems are not found in the literature.

The author of the thesis improved and modified the main PM modelling software (originally written by colleagues Gundars Ratnieks and Andis Rudevičš for FZ, then supplemented by Andrejs Sabanskis, Armands Krauze, Matīss Plāte), and used this software for parameter studies. The author wrote scripts for simplified estimations (see Sections 3.1 and 3.3.1), created a new solver using *OpenFOAM C++* library implementing volume of fluid method for moving the melting interface (see Section 2.4.1), and created the inductor optimization program using *Python* (see Section 2.5). The author also communicated with industry partners (Anatoly Kravtsov from *KEPP EU*, *Mašīnbūves Kompetences centrs*) about system parameters, project results and practical aims of the work. All numerical simulations that are presented below were run by the author.

Based on the obtained results, the author of the thesis wrote four scientific papers as a main author: [Dis1], [Dis2], [Dis3], [Dis4], and a part of another paper as a contributing author [Dis5]. The results were presented at internetational conferences [Conf1], [Conf2], [Conf3], [Conf4], [Conf5], and the conferences of University of Latvia [Conf6], [Conf7], [Conf8], [Conf9].

The present thesis was created during and after the doctoral studies at University of Latvia, Riga, 2015–2023.

1.5 The goal and the tasks of the work

The literature review showed that some publications mention a limit of 20 mm [33, 45] or 40 mm [46] on the diameter of crystals grown by the pedestal method. However, nowadays the demand in the silicon crystal market exists mainly for large diameters[3], starting with 100 mm. The pedestal method has not been modelled earlier due to its low popularity, and also due to the advantages of floating zone method for the large diameter silicon crystal growth.

The goal of the work is **to demonstrate (using numerical modelling) the possibility of large diameter (100 mm) silicon crystal growth with pedestal method, and to provide practical advises for the design of the corresponding experimental apparatus and process realization**. This goal was reached by performing the following tasks:

1. Create the software for the modelling of PM, which is based on the software for FZ simulations, previously developed in the Institute of Numerical Modelling.
2. Test the software and improve it in accordance with the development of experimental setup by industrial partner *KEPP EU*.
3. Verify the software by comparing simulation results to the available experiments.
4. Optimize the shape of high-frequency inductor for the growth of crystals with 100 mm diameter.

1.6 Thesis

The modelling results affirm that it is possible to grow large (100 mm in diameter) silicon crystals, if advancements of pedestal process are made.

1.7 Approbation of results

Author's publications

[Dis1] K. Surovovs, A. Kravtsov, and J. Virbulis, "Numerical Modelling for the Diameter Increase of Silicon Crystals Grown with the

[3]The larger crystal diameter is, the more microschemes can be simultaneously produced from one crystal wafer.

Pedestal Method," *Journal of Crystal Growth*, vol. 563, p. 126095, 2021.

[Dis2] K. Surovovs, A. Kravtsov, and J. Virbulis, "Modelling of the Pedestal Growth of Silicon Crystals," *Lithuanian Journal of Physics*, vol. 61, no. 3, pp. 151–156, 2021.

[Dis3] K. Surovovs, A. Kravtsov, and J. Virbulis, "Optimization of the Shape of High-Frequency Inductor for the Pedestal Growth of Silicon Crystals," *Magnetohydrodynamics*, vol. 55, no. 3, pp. 353–366, 2019.

[Dis4] K. Surovovs, M. Plāte, and J. Virbulis, "Modelling of Phase Boundaries and Melt Flow in Crucible-Free Silicon Crystal Growth Using High-Frequency Heating," *Magnetohydrodynamics*, vol. 53, no. 4, pp. 715–721, 2017.

[Dis5] A. Kravtsov, K. Surovovs, and J. Virbulis, "Float Zone Single Crystals for Testing Rods, Pulled under Electron Beam Heating," in *IOP Conference Series: Materials Science and Engineering*, vol. 503, 2019.

The author's publications, that are not included in the Doctoral Thesis, are listed below:

- K. Surovovs, M.Surovovs, A. Sabanskis, J. Virbulis, K. Dadzis, R. Menzel and N. Abrosiov, "Numerical Simulation of Species Segregation and 2D Distribution in the Floating Zone Silicon Crystals". *Crystals*, vol. 12(12), 1718, 2022.
- A. Sabanskis, K. Surovovs and J. Virbulis, "3D Modeling of Doping From the Atmosphere in Floating Zone Silicon Crystal Growth". *Journal of Crystal Growth*, vol. 457, pp. 65–71, 2017.
- A. Sabanskis, K. Surovovs, and J. Virbulis, "Three-dimensional Modelling of Dopant Transport in Gas and Melt During FZ Silicon Crystal Growth". *Magnetohydrodynamics*, vol. 51, pp. 157–170, 2015.
- A. Sabanskis, K. Surovovs, A. Krauze, M. Plāte, and J. Virbulis, "Modelling of the Influence of Electromagnetic Force on Melt Convection and Dopant Distribution at Floating Zone Growth of Silicon". *Magnetohydrodynamics*, vol. 51, pp. 375–384, 2015.
- K. Surovovs, A. Muiznieks, A. Sabanskis, and J. Virbulis, "Hydrodynamical Aspects of the Floating Zone Silicon Crystal Growth Pro-

cess". *Journal of Crystal Growth*, vol. 401, pp. 120–123, 2014.

- K. Surovovs, V. Valle, A. Sorokins, J. Timošenko, D. Docenko, A. Cēbers and D. Bočarovs, "Latvijas 42. atklātā fizikas olimpiāde". *Zvaigžņotā debess*, vol. 238, pp. 52–59, 2017.

Author's participation in conferences

[Conf1] K. Surovovs, M. Surovovs, A. Sabanskis, J. Virbulis, K. Dadzis, R. Menzel, and N. Abrosimov, "Effect of Melt Flow on Dopant and Impurity Segregation During Floating Zone Growth of Silicon," in *7th European Conference on Crystal Growth*. Paris, France, July 2022.

[Conf2] K. Surovovs, A. Kravtsov, and J. Virbulis, "Modelling of the Pedestal Growth of Silicon Crystals," in *Electromagnetic Processing of Materials*. Riga, Latvia, June 2021.

[Conf3] K. Surovovs, A. Kravtsov, and J. Virbulis, "Modelling of the Pedestal Growth of Silicon Crystals," in *Functional Materials and Nanotechnologies*. Vilnius, Lithuania, November 2020.

[Conf4] K. Surovovs, A. Kravtsov, A. Sabanskis, and J. Virbulis, "Optimization of the Inductor Shape for the Pedestal Growth of Silicon Crystals Using Mathematical Modelling," in *Sixth European Conference on Crystal Growth*. Varna, Bulgaria, September 2018.

[Conf5] K. Surovovs and J. Virbulis, "The Modelling of Phase Boundaries and Melt Flow in the Crucible-Free Silicon Crystal Growth Using High-Frequency Induction Heating," in *VIII International Scientific Colloquium "Modelling for Materials Processing"*. Riga, Latvia, September 2017.

[Conf6] K. Surovovs, A. Kravtsov, and J. Virbulis, "Heterogēna sildīšanas sistēma Si kristālu audzēšanai ar pjedestāla metodi," in *LU 80. conference*. Riga, Latvia, January 2022.

[Conf7] K. Surovovs, A. Kravtsov, and J. Virbulis, "Kušanas frontes formas uzlabošana Si kristālu audzēšanā no pjedestāla," in *LU 77. Zinātniskās konferences sekcija "Matemātiskās metodes pētījumu izcilībai"*. Riga, Latvia, January 2019.

[Conf8] K. Surovovs, A. Sabanskis, A. Kravtsov, and J. Virbulis, "Silīcija audzēšanas no pjedestāla matemātiskā modelēšana ar mērķi

palielināt kristāla diametru," in *LU 76. Zinātniskās konferences sekcija "Matemātiskās metodes pētījumu izcilībai"*. Riga, Latvia, February 2018.

[Conf9] M. Plāte and K. Surovovs, "Modelēšana silīcija kristālu audzēšanas procesam ar beztīģeļa induktīvu kausēšanu," in *LU 75. Zinātniskās konferences sekcija "Matemātiskās metodes pētījumu izcilībai"*. Riga, Latvia, February 2017.

Author's participation in projects

The present thesis is based on the results obtained in the following ERDF projects, where the author and his supervisor collaborated with *KEPP EU* [35]:

- "Technological research and production of silicon with a diameter of up to 100 mm for use in power rectfiers" – ERDF "Competence Centre for Mechanical Engineering", Id. Nr. 1.2.1.1/18/A/008.
- "Investigating the growth of silicon dislocation-free single crystals from a pedestal" – ERDF "Competence Centre for Mechanical Engineering", Id. Nr. 1.2.1.1/16/A/003.

The work on the present thesis is supported also by the following project:

- "Strengthening the capacity of the UL PhD programme in the new doctoral model" – University of Latvia, Id. Nr. 8.2.2.0/20/I/006.

2 Mathematical models

The detailed description of calculation procedures is published in [62] and [63], therefore the previously developed models are only briefly summarized, and the newly introduced ones (Sec. 2.2, 2.4.1, 2.5) are described in more details. EM field simulations are coupled with the phase boundary simulations and consist of two different parts: high-frequency (HF, typically 1–3 MHz) and middle-frequency (MF, typically 50–100 kHz) fields.

2.1 High-frequency EM field

Small skin layer δ ($\delta = 1.4$ mm in the solid near the Si melting point for the HF inductor frequency $f_{\mathrm{HF}} = 2.6$ MHz) allows to use HF approximation for the main inductor EM field calculations. The model is implemented using the boundary element method and published in [54]. An example of calculated magnetic field and induced heat density is shown in Fig. 2.1.

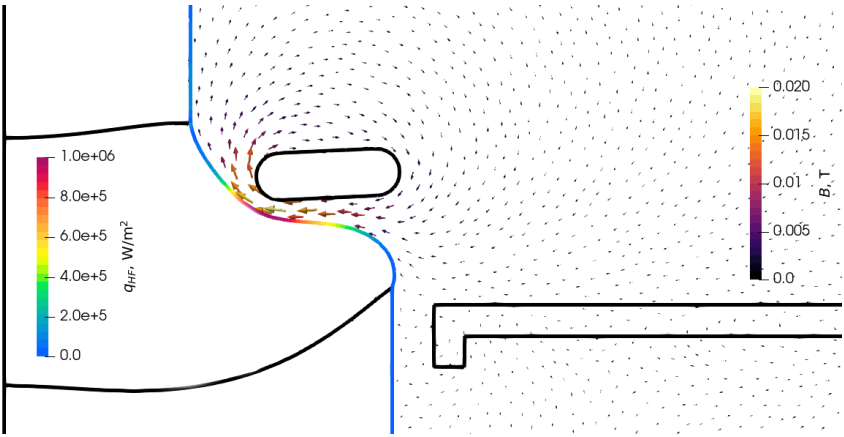

Figure 2.1. Induced EM heat surface density on silicon surfaces q_{HF} and magnetic field B that is created by the high-frequency inductor. A simulation example with crystal diameter $D_C = 36$ mm and pedestal diameter $D_P = 75$ mm.

2.2 Middle-frequency EM field

For the MF field calculations, *GetDP* program is used [64]. It solves the equation for vector potential $\vec{A}$ in all volumes (including the gas domain, disregarding chamber walls due to assumption that they are sufficiently far away):

$$\nabla \times \nabla \times \vec{A} = \mu_0 \sigma(-i\omega\vec{A}) + \mu_0 \vec{J}, \tag{2.1}$$

where $\mu_0 = 4\pi \cdot 10^{-7}$ H/m, $\omega = 2\pi f_{\mathrm{MF}}$ is the angular frequency, $\vec{J}$ – current density in the MF inductor, and σ – the electrical conductivity of silicon: $1.2 \cdot 10^6$ S/m for liquid phase and temperature-dependent conductivity with $3.3 \cdot 10^4$ S/m at the melting point for solid phase [65]. Due to the axial symmetry, $\vec{A}$ has only azimuthal component: A_φ. Boundary conditions are $A_\varphi = 0$ on the system axis and zero normal gradient of A_φ on the boundaries of gas domain. The induced heat source density is being calculated as

$$q_{\mathrm{MF}} = \frac{j^2}{2\sigma} = \frac{\sigma E^2}{2} = \frac{\sigma}{2}\omega^2 A^2, \tag{2.2}$$

where j, E, A are magnitudes of induced current density, electric field, and vector potential. An example of MF magnetic field and induced heat, calculated with $f_{\mathrm{MF}} = 100$ kHz, is shown in Fig. 2.2.

2.3 Heat transfer and phase boundaries

For the temperature field T, the steady heat transport equation is solved, using MF and HF induced heat sources. Despite the crystal pulling, the process can be considered quasi-stationary (i.e., phase boundaries do not move in the laboratory reference frame) during the cylindrical phase, when crystal diameter does not change in time, and the temperature distribution remains steady. By default, melt motion has not been taken into account, and only later was analyzed with a specific program (Sec. 2.4.1). The shape of phase boundaries is calculated in the following way:

- Melting and crystallization interfaces are being moved according to heat balance at nodes (in other words, locally using a 1D solution of the Stefan problem), until quasi-stationary shape of phase boundaries is reached.
- The shape of the free melt surface is obtained such that it equilibrates hydrostatic pressure, EM induced pressure and surface tension.

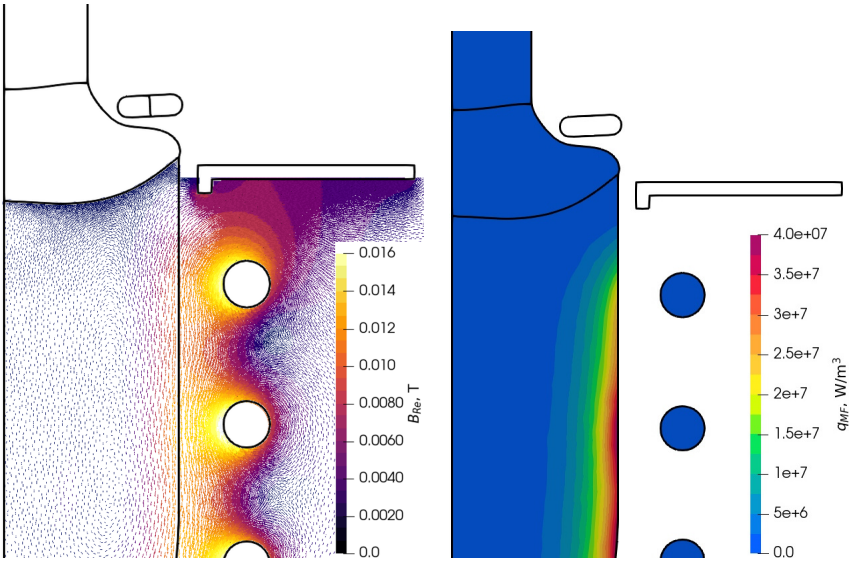

(a) Middle-frequency magnetic field, real part

(b) Induced heat density in silicon

Figure 2.2. An example of the results of middle-frequency EM field modelling for crystal diameter $D_C = 36$ mm and pedestal diameter $D_P = 75$ mm.

- The outer surfaces of crystal and pedestal are not being moved, only "prolonged" until intersection with the melting or crystallization front.

The value of inductor current, that ensures user-prescribed height of the external triple point (ETP, see Fig. 1.2), is found by the proportional-integral-derivative (PID) algorithm. A more detailed description of the model for heat transfer and phase boundaries (in the case of FZ method) is presented in [62].

2.4 Melt flow

The first model of melt flow considers fixed phase boundaries. It imposes incompressible laminar Navier-Stokes equation for the melt velocity, with Boussinesq approach for the thermal convection. Marangoni force density, using Marangoni coefficient $M = 2 \cdot 10^{-4}\,\mathrm{N/m{\cdot}K}$, and EM force density are considered on the free surface. Standard convection-diffusion equation is used for the simulation of melt temperature, with EM induced

heat and radiation as boundary conditions. This model is implemented using *OpenFOAM* software library and described (in the case of FZ method) in [63].

2.4.1 Non-stationary melting interface

To take Si melting into account, in some cases the second melt flow model is used: the first model is complemented with phase variable f_c, that changes from 0 (melt) to 1 (solid Si), as shown in Eq. (2.3), where $T_0 = 1687$ K is Si melting temperature. The solidification is modelled by increasing melt viscosity, as well as decreasing its density and heat conductivity, for high f_c. The latent heat is taken into account as a heat source $\rho L \frac{\partial f_c}{\partial T} \frac{\partial T}{\partial t}$ in the convection-diffusion equation for the silicon temperature T (where ρ is silicon density, L – specific latent heat of silicon melting and t – time). "Smearing interval" ΔT, where f_c changes linearly depending on T, was decreased, until the solution was not dependent on it. In this way, $\Delta T = 0.5$ K was obtained.

$$f_c(T) = \begin{cases} 0, & \text{for } T > T_0 + \frac{\Delta T}{2} \\ \frac{1}{\Delta T}(T_0 + \frac{\Delta T}{2} - T), & \text{for } T_0 - \frac{\Delta T}{2} < T < T_0 + \frac{\Delta T}{2} \\ 1, & \text{for } T < T_0 - \frac{\Delta T}{2} \end{cases} \tag{2.3}$$

The presence of the crystal was modelled by setting constant temperature gradient of 5 K/mm at the center of the upper surface of the calculation domain, which consisted of pedestal (where $f_c = 1$) and melt (where $f_c = 0$). On the other surfaces of the domain, radiative heat losses and EM induced heat sources were set.

2.5 Optimization of high-frequency inductor

During the phase boundary calculations (see Sec. 2.3), the inductor current is automatically adjusted to maintain a prescribed ETP height. In other words, the current value is being fitted to ensure that the pedestal melts at the rate required for a quasi-stationary process. The inductor frequency is kept constant during all iteration of the optimization algorithm because it is determined by experimental considerations such as the generator design. Therefore, only the geometrical parameters of the HF inductor are optimized in this work.

The HF inductor is assumed to be axially symmetrical, and its shape is parameterized as shown in Fig. 2.3: $r_{\mathrm{ind}}, z_{\mathrm{ind}}$ are radial and axial coor-

dinates of the center of inductor cross-section, $2k_{\mathrm{ind}}$ – cross-section length, c_{ind} – curvature radius, and α_{ind} is the cross-section inclination angle.

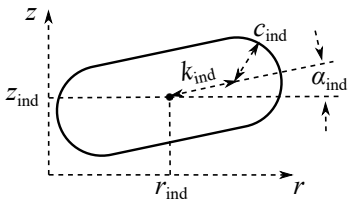

Figure 2.3. Scheme of the high-frequency inductor cross-section parameters, that were used for its optimization.

The target function is selected to be melt height H_M (see Fig. 1.2(b)). Such selection ensures maximal molten region between solid rods, which helps to mitigate one of the main issues when large crystals are grown – melt center freezing [46]. The optimization was performed with the gradient method. The optimization algorithm considered the direction of H_M increase, denoted by ∇H_M, in the inductor parameter phase space (r_{ind}, z_{ind}, c_{ind}, k_{ind}, α_{ind}). Optimization algorithm steps are listed below:

1. using the program for the modelling of phase boundaries, compute H_M with some set of inductor parameters (i.e., a point in the parameter space) $\vec{p} = (r_{\mathrm{ind}},\ z_{\mathrm{ind}},\ c_{\mathrm{ind}},\ k_{\mathrm{ind}},\ \alpha_{\mathrm{ind}})$, further denoted by $H_M(\vec{p})$; if a calculation diverges, assume that $H_M = 0$;
2. compute five values of H_M for five sets of parameters: $\vec{p_r}$, $\vec{p_z}$, $\vec{p_c}$, $\vec{p_k}$, $\vec{p_\alpha}$, that are shifted from $\vec{p}$ by distance $d = 0.01$ mm, each in the corresponding direction;
3. calculate $\nabla H_M = \sum_i \dfrac{H_M(\vec{p_i}) - H_M(\vec{p})}{d}\vec{e_i}$, where i is a coordinate from the set $\{r_{\mathrm{ind}}\,,\ z_{\mathrm{ind}},\ c_{\mathrm{ind}},\ k_{\mathrm{ind}},\ \alpha_{\mathrm{ind}}\}$ and $\vec{e_i}$ – corresponding base vector in the phase space;
4. calculate the step $\vec{s} = s_0 \dfrac{\nabla H_M}{|\nabla H_M|}$, where s_0 is step magnitude (user-defined before the start of the algorithm, usually in order of 1 mm);
5. compute H_M with the parameter set $(\vec{p}+\vec{s})$; if $H_M(\vec{p}+\vec{s}) < H_M(\vec{p})$, then decrease s_0 twice and repeat from step 4.;
6. change the position in the parameter space from $\vec{p}$ to $\vec{p}+\vec{s}$;
7. repeat from step 1. until the convergence criterion is reached.

3 Simulation results

3.1 Free surface shape estimations

A simplified estimations of the shape of the free melt surface and its comparison to FZ case has been performed[1] in [Dis3]. In these estimations, only surface tension and gravitational forces were taken into account. The surface shape can be described in cylindrical coordinates r and z by the Laplace–Young equation in a specific form [48]:

$$r'(s) = \sin\phi(s), \tag{3.1}$$

$$z'(s) = \cos\phi(s), \tag{3.2}$$

$$\phi'(s) = \frac{\cos\phi(s)}{r(s)} + \frac{\rho g(z(s) - z_0)}{\gamma}, \tag{3.3}$$

where s is the arc length: $\mathrm{d}s = \sqrt{\mathrm{d}r^2 + \mathrm{d}z^2}$, ϕ is the angle between the free surface and the vertical, $\rho = 2580$ kg/m^3 is silicon density, $g = 9.81$ m/s^2 is the acceleration of gravity, $\gamma = 0.88$ N/m is silicon surface tension, and z_0 is a melt volume controlling parameter (this parameter is not known, i.e., melt volume can be different; therefore z_0 was iteratively adjusted to maximize zone height). To model cylindrical crystal growth, $\phi = 11°$ angle [28] was imposed at the internal triple point (ITP) for PM (see the scheme in Fig. 1.2), and the external triple point (ETP) for FZ systems. Do to stabilizing effect of EM pressure [66], which is neglected in this estimation, the obtained zone shapes (see Fig. 3.1(a)) are worst-case estimates of possible zone height $z_{\max}$ (large $z_{\max}$ reduces the risk of melt freezing).

The main conclusion is that the maximum zone height – 17 mm for FZ, 15 mm for PM – can be reached if the ratio of ETP and ITP radii is at least 2. It is also shown that $z_{\max} = 0$ (and therefore the growth process is not possible) when $r_{\mathrm{ETP}} = r_{\mathrm{ITP}}$ in PM.

3.2 The system without side heating: reflector instead of heater

3.2.1 Shape of phase boundaries

At the beginning of the research, the necessity of the side heater was not known, and copper reflector was used instead of the later used MF side

[1] Here and further, figures and text fragments from author's publications are used.

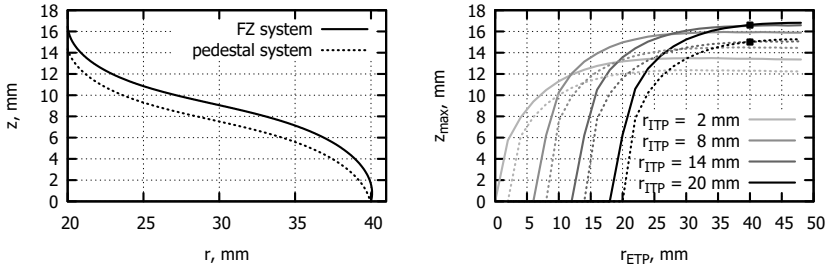

(a) Calculated shapes of the free surface for $r_{\mathrm{ETP}} = 40$ mm and $r_{\mathrm{ITP}} = 20$ mm

(b) Maximal possible zone height $z_{\max}$ with different r_{ETP} and r_{ITP}

Figure 3.1. The results of free surface shape estimations: calculated free surface shape and zone height in the floating zone system (solid lines) and the pedestal system (dotted lines). The corresponding calculations from the left image are marked with squares on the right image. The radii of the external triple point and internal triple point are denoted with r_{ETP} and r_{ITP}.

heater (see Fig. 3.2(a)). For the first simulations, crystal diameter $D_C = 12$ mm and pedestal diameter $D_P = 85$ mm were selected. The (b) side of the figure shows the phase boundaries, calculated with different inductor frequencies f_{HF} from 440 to 2640 kHz. Distance between inductor and melt increases for lower f_{HF} due to the increase in EM pressure. The upper surface of the pedestal is not completely melted, because the cylindrical growth had not been considered at that stage. These boundaries were used to generate meshes for the melt flow calculations, described in the next section.

3.2.2 Melt flow

Stationary shape of phase boundaries

The melt flow model (i.e., the hydrodynamic model, the first model from Sec. 2.4) demonstrated that higher frequencies lead to smaller melt velocity (Fig. 3.3(b)) and thus higher temperature maximum (Fig. 3.3(a)). The azimuthal component of velocity is negligible, because crystal and pedestal were not rotating in this case. The more detailed analysis of the frequency influence is shown in Fig. 3.4. Due to smaller inductor current (Fig. 3.4(a)) and melt velocity (b), higher f_{HF} are more favorable for the system. However, the voltage is higher (c), and the generator is more expensive, for higher frequency. Maximal temperature in the cal-

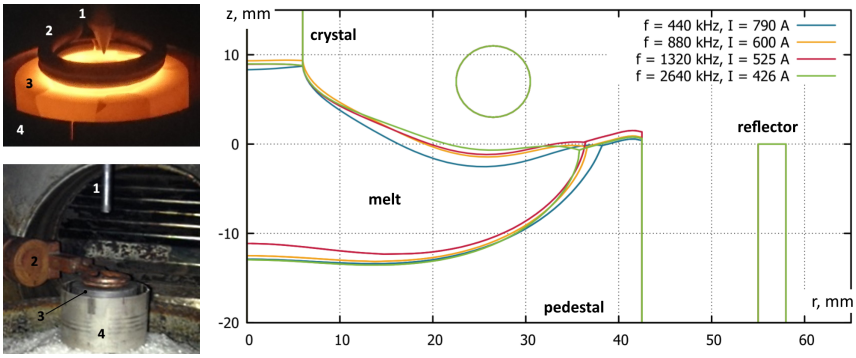

(a) **(b)**

Figure 3.2. (a) – photographs of the system without side heating (reflector instead of side heater) with seed crystal 1, high-frequency inductor 2, pedestal 3, and reflector 4. (b) – the shape of phase boundaries, calculated with different inductor frequencies f and inductor currents I.

culations with melt flow ((d), yellow lines) is much lower, than without it (i.e., obtained with the heat transfer and phase boundary model only, described in Sec. 2.3). The influence of melt flow is so large because intensive convection, both thermal and electromagnetically created, is present in the system. This convection radically increases maximal heat flux at the melting front (e), therefore it is necessary to investigate the melt flow influence on the shape of the melting interface.

Non-stationary melting interface

The induced convective heat transfer is 2-3 times more intensive than the conductive heat transfer (see Fig. 3.4(e)). It means that the melt flow can have significant effect on phase boundaries. Therefore, the melt flow model with non-stationary melting interface was created using volume-of-fluid method, as described in Sec. 2.4.1. This model allowed to describe transient features of the melt motion, including the initial melting of the pedestal, see Fig. 3.5. Melt motion rapidly develops and is very chaotic, the vortex can even change its direction from clockwise to counter-clockwise, e.g. at $t = 110$ s. However, this test demonstrated that the pedestal height $H_P = 40$ mm is too small, because the pedestal bottom can probably melt due to intensive jet of hot Si. A longer pedestal ($H_P = 60$ mm) was selected for the next calculations, in order to prevent the melting of pedestal bottom surface.

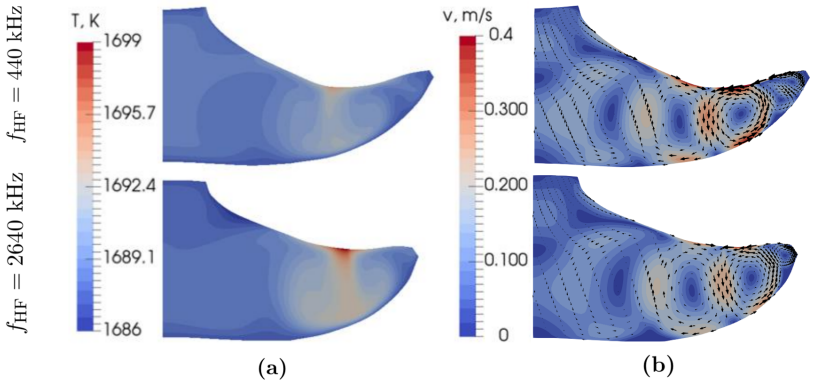

Figure 3.3. Melt temperature T (a) and velocity v (b), calculated using the inductor frequencies $f_{\mathrm{HF}} = 440$ kHz (top) and $f_{\mathrm{HF}} = 2640$ kHz (bottom), with crystal diameter $D_C = 12$ mm and pedestal diameter $D_P = 85$ mm.

The calculated silicon temperature and velocity are shown in Fig. 3.6(a). In the experimental growth it is beneficial to have large height of the molten region, to prevent the freezing of its central part. However, the molten region height H_M cannot be observed directly. Correlation between temperatures at different points on the pedestal surface and molten region size was analyzed, because it could aid the control of the growth experiment. It was concluded that the temperature of the point located 40 mm below the pedestal rim is the best proxy for evaluating H_M, see Fig. 3.6(b).

PID control

The previously described simulations were performed with fixed value of electric current I in the HF inductor (Fig. 3.5), or with manual stepwise change of I (Fig. 3.6). However, in the cylindrical stage of real crystal growth processes heating power is usually being controlled to ensure that a particular geometric parameter is unchanged (i.e. zone height in FZ process). In the case of the pedestal method, ETP vertical coordinate z_{ETP} was selected as a controlled parameter, with a user-defined target $z_{\mathrm{ETP},\,0}$. A proportional–integral–derivative (PID) controller was used:

$$e(t) = z_{\mathrm{ETP}}(t) - z_{\mathrm{ETP},\,0}(t), \tag{3.4}$$

$$\Delta I(t) = K_p \left(e(t) + K_i \int_0^t e(\tau)\,\mathrm{d}\tau + K_d \frac{\mathrm{d}e(t)}{\mathrm{d}t} \right), \tag{3.5}$$

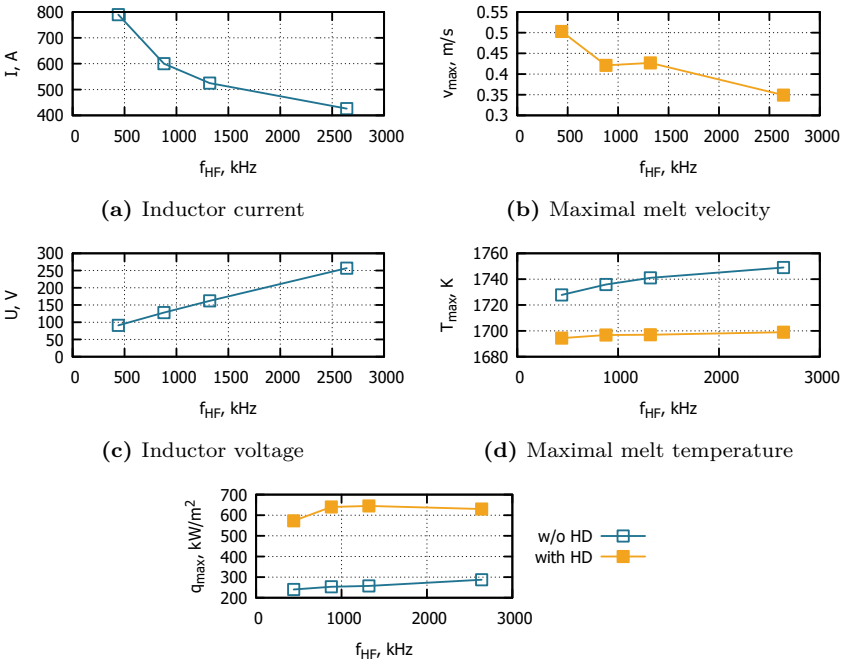

(a) Inductor current

(b) Maximal melt velocity

(c) Inductor voltage

(d) Maximal melt temperature

(e) Maximal heat flux through the melting front

Figure 3.4. The influence of inductor frequency f_{HF} in simulations without hydrodynamics (blue color) and with hydrodynamics (yellow color), obtained with crystal diameter $D_C = 12$ mm and pedestal diameter $D_P = 85$ mm.

where $e(t)$ is the difference between the actual ETP coordinate and ETP coordinate target, ΔI is the change of inductor current, and $(K_p,\ K_i,\ K_d)$ are controller coefficients. The convergence of inductor current is shown in Fig. 3.7, and it shows that it is necessary to use all three parts of the controller: the integral part helps to reach the target ETP height faster, the derivative part dampens oscillations. The optimal values that ensure rapid convergence to quasi-stationary solution were found to be $K_p = 80$ A/mm, $K_i = 0.1$ 1/s, $K_d = 10$ s.

Inductor optimization: successive method

Inductor optimization requires a very large amount of calculations. Each iteration of the algorithm requires several phase boundary simulations to obtain the melt height for different inductor changes. These sim-

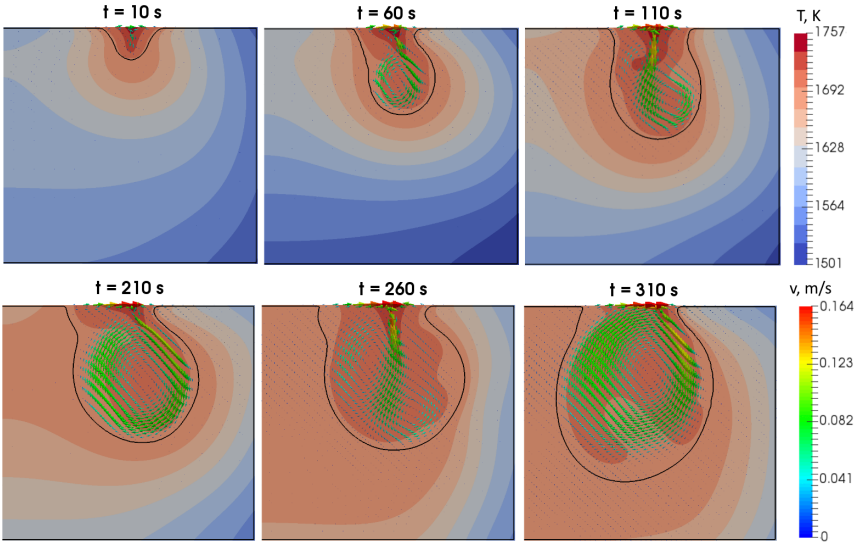

Figure 3.5. Silicon temperature T and velocity v at different time instants (time from the beginning of the process, inductor power assumed to be constant). Pedestal height $H_P = 40$ mm and diameter $D_P = 80$ mm.

ulations have to be repeated in each subsequent iteration, and the total number of simulations is several dozens for one system and several hundreds for all the systems considered in this work. An even larger number of simulations were carried out for other project tasks and are not included in this thesis. Therefore, despite the large influence of melt flow, melt motion is not considered in this section and all subsequent sections, in order to increase the computation speed and to allow for more extensive parametric studies.

The present subsection and the two next subsections describe the simulations of the system with the following parameters: crystal diameter $D_C = 36$ mm, pedestal diameter $D_P = 75$ mm (it was selected based on simplified estimation of optimal diameter ratio from Sec. 3.1), crystal pulling velocity $v_p = 2$ mm/min, HF inductor frequency $f_{\mathrm{HF}} = 2.64$ MHz.

Designation of inductor parameters is provided in Fig. 2.3. The method consisted of adjusting r_{ind} and z_{ind} (for fixed $c_{\mathrm{ind}}, k_{\mathrm{ind}}, \alpha_{\mathrm{ind}}$), then finding optimal value of c_{ind} (while other parameters are fixed), and finally adjust k_{ind} and α_{ind} (while other parameters are fixed). The advantages of the successive method (in comparison with the gradient method) are

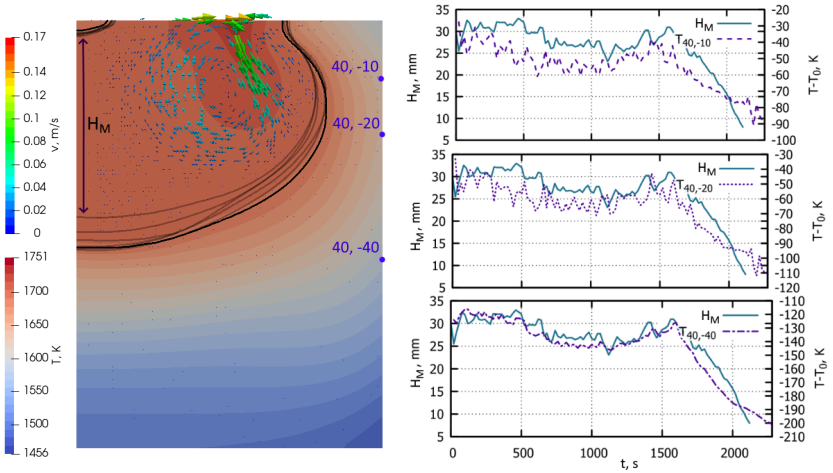

(a) Silicon temperature and velocity at a selected time moment, melting front shapes from other moments shown with gray lines

(b) The connection between molten region height H_M and silicon temperatures at different points of pedestal side surface

Figure 3.6. Non-stationary modelling of melting interface, pedestal height $H_P = 60$ mm and diameter $D_P = 80$ mm.

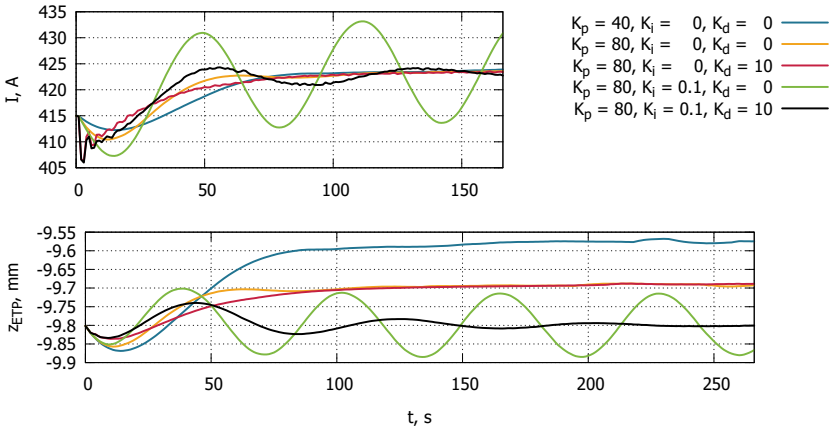

Figure 3.7. Evolution of inductor current I (top) and ETP vertical coordinate z_{ETP} (bottom) with different parameters of PID controler, see Eq. (3.5).

simplicity and possibility to cover a large range of parameters.

First simulations were run with $k_{\text{ind}} = \alpha_{\text{ind}} = 0$, $c_{\text{ind}} = 4$ mm, and different $r_{\text{ind}}, z_{\text{ind}}$ (see Fig. 3.8(a)), however only part of them converged (10 of 64), and only few of the converged simulations are shown for convenience. The other simulations diverged either because of the melt freezing (when the inductor radius r_{ind} was too big) or because of the melt spilling over the pedestal edge (when the inductor was located too far from the ETP). The range that was covered by cross-sections of the considered inductor shapes is colored in gray.

The next step of the successive method was to select the case with the largest H_M and to optimize other inductor parameters. A wide range of c_{ind} was tested, and the converged simulation showed no visible influence, see Fig. 3.8(b). Then different k_{ind} and α_{ind} were used, and few of them are shown in Fig. 3.8(c). It can be concluded the increase of k_{ind} increases H_M sensitivity on α_{ind}. The largest H_M obtained by the successive method was 12.0 mm, which corresponded to horizontal ($\alpha_{\text{ind}} = 0$) and elongated ($k_{\text{ind}} = 2$ mm) inductor cross-section. However, this method does not ensure that even local maximum of H_M is reached.

Inductor optimization: gradient method

The gradient method is described in Sec. 2.5. This method has converged (see Fig. 3.9) and performed slightly better than the successive method, leading to $H_M = 12.2$ mm. Unfortunately, despite successful convergence of all simulations, the changes of the inductor coordinates suggested by the gradient method were smaller than 1 mm, and inductor cross-sections covered much smaller parameter range than in the successive method. It illustrates the fact that only the local maximum of H_M can be found with the gradient method, thus the final inductor shape depends strongly on the initial inductor parameters (more comments on this dependence are made in the next section). The comparison of these results to the previously calculated phase boundaries, shown in Fig. 3.8, also demonstrates that the algorithm has not considered wide enough range of parameters, e.g. k_{ind} has not increased significantly, and the cross-section remained circular.

The optimization was performed also for two other systems: with $D_C = 60$ mm and $D_C = 90$ mm [Dis3], however these results are not shown here for the sake of brevity, because analogous results are included in the next section, where the full crystal growth system is considered.

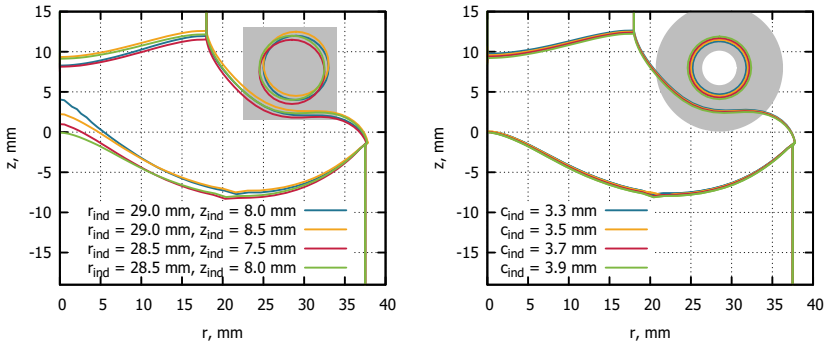

(a) Optimizing coordinates of inductor cross-section center $r_{\text{ind}}, z_{\text{ind}}$

(b) Optimizing inductor cross-section radius c_{ind} only

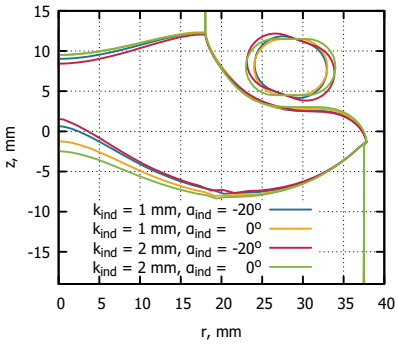

(c) Optimizing inductor cross-section length and inclination $k_{\text{ind}}, \alpha_{\text{ind}}$

Figure 3.8. Phase boundaries obtained during the inductor optimization with successive method.

3.3 The system with simplified pedestal side heating

In the first experiments, KEPP EU company used a copper reflector placed around an 85 mm diameter pedestal, see Fig. 3.2. These experiments demonstrated that the heat induced by the HF inductor was not sufficient: the top surface of the pedestal was not completely melted. Unlike the numerical model, where the power of the HF inductor was not limited, the high-frequency generator [32] used in the experiment could not provide the required current value. Given that the numerical model also predicted difficulties in melting the upper surface of larger pedestals,

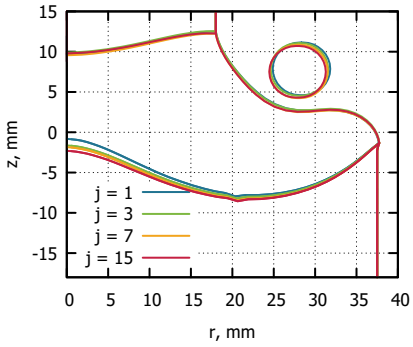

(a) Phase boundaries

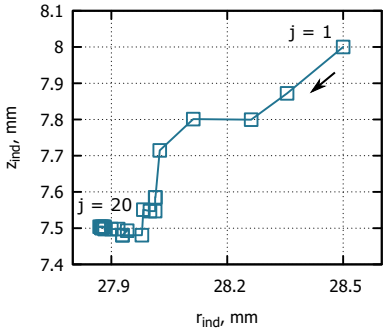

(b) Inductor cross-section center coordinates r_{ind} and z_{ind}

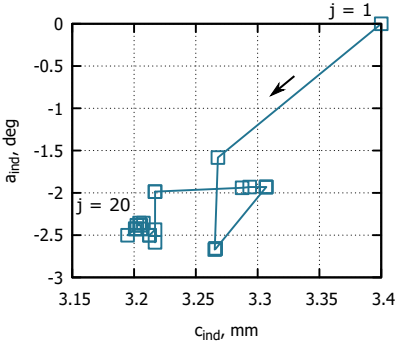

(c) Inductor cross-section inclination angle α_{ind} and curvature radius c_{ind}

Figure 3.9. The convergence of phase boundaries (a) and inductor parameters (b, c) during the gradient method, where j is the method iteration number.

we concluded that pedestal side heating was necessary.

3.3.1 Evaluation of optimal side heater position

In the beginning of the project, the side heating was modelled in a simplified way, by setting uniform heat flux density at the pedestal side. The main goal was to find the approximate position and power of the heater, that is the most suitable for transferring heat to the pedestal center (because it was experimentally shown that the power induced by HF inductor is not enough [32]). The system was assumed to be axially symmetric. Heating region has height H_Q mm, which is located z_Q mm from the ETP

(see Fig. 3.10(a)).

The parameters of the standard calculation case are given in Tab. 3.1. The thermal dependence of thermal conductivity and silicon emissivity is neglected for simplicity, as the main region of interest is near the top of the pedestal.

Table 3.1. Summary of the geometrical parameters and material properties, used for the optimal side heater position evaluation.

Pedestal height H_P	240 mm
Pedestal radius R_P	40..100 mm
Heating region height H_Q	30 mm
Heating region distance to ETP z_Q	10..100 mm
Integral heat flux Q	2 kW
Ambient temperature T_{amb}	1000 K
Silicon emissivity ε	0.6
Thermal conductivity λ	26 $\mathrm{W/_{m \cdot K}}$

Constant heat flux $q = \lambda \dfrac{\partial T}{\partial r} = \dfrac{Q}{S_Q} = \dfrac{Q}{2\pi R_P H_Q}$, where S_Q is the heating region area and R_P is the pedestal radius, was set at the heating region. At the bottom pedestal surface, fixed temperature boundary condition $T = 1000$ K was used to ensure calculation convergence. On the other boundaries, radiation boundary conditions were set. The standard temperature diffusion equation $\nabla^2 T = 0$ was solved, *FEMM* program with the *Mathematica* interface [67] was used. Some examples of calculation results, showing temperature field in the pedestal, are shown in Fig. 3.10(b).

Temperatures at the center of the pedestal upper surface and at its rim (T_{cen} and T_{rim}) depended on the heated region position z_Q in different ways, as shown in Fig. 3.11(a). The rim temperature decreased faster than the center temperature, because the heating was applied at the pedestal side, i.e. closer to the ETP than to the pedestal center. Due to different rates of temperature decrease, dependence of $\Delta T = T_{\mathrm{cen}} - T_{\mathrm{rim}}$ is not monotonous, see Fig. 3.11(b).

As the goal of this study was to increase center heating, the systems with the maximal ΔT are the most beneficial. It can be concluded that the optimal distance z_Q should be ~ 30 mm for the pedestal with 40 mm radius. This distance increases to $\sim$ 50 mm for $R_P = 60$ mm and to

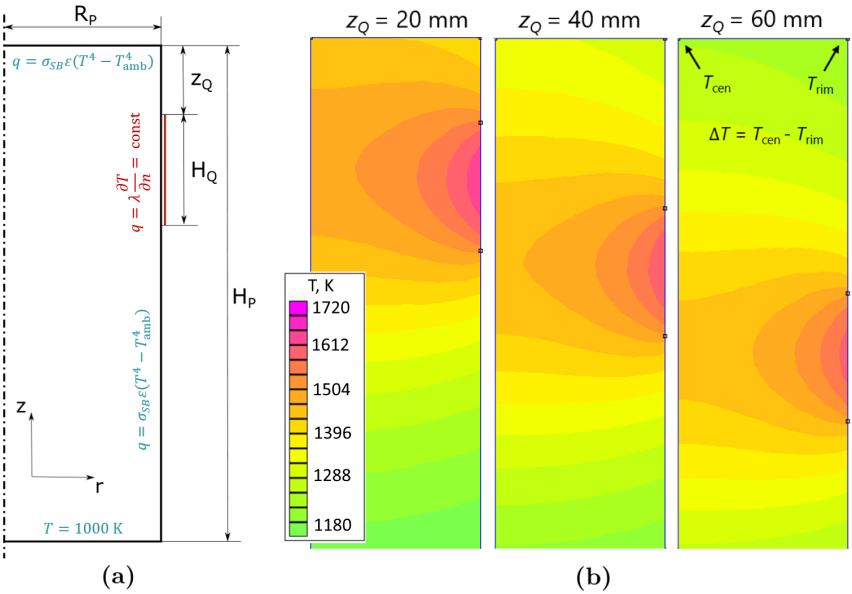

Figure 3.10. (a) – the scheme of the used geometry and boundary conditions (vertical size is not shown in full scale). (b) – calculation examples for pedestal radius $R_P = 40$ mm, $Q = 2$ kW, and different positions of heated area z_Q.

80..100 mm for $R_P = 100$ mm. These results were used to start initial parameter studies for the systems with simplified side heating, described in Sec. 3.3. The model is not suitable for the later developed MF inductor (Sec. 2.2), though, because its induced power is distributed inside the pedestal, not only on its surface.

3.3.2 Phase boundaries and HF inductor optimization

The side heating was firstly included in the model in a simplified way: constant heat flux density was set on 30 mm thick stripe of the pedestal side surface, 20 mm below the ETP. The application of total $Q = 1$ kW heating power significantly increased pedestal temperature, and it made melt height much larger, see Fig. 3.12. As large part of the heat needed to melt the pedestal is supplied from its side, the HF inductor does not have to maintain the same current as without the side heating, and its current decreases by 20%. Therefore, less heat is induced on the free surface, and the maximal melt temperature is lower in the case of the side heating.

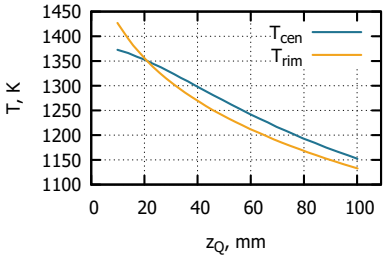

(a) Temperature in the center of the pedestal upper surface T_{cen} and at the rim T_{rim} with pedestal radius $R_P = 60$ mm

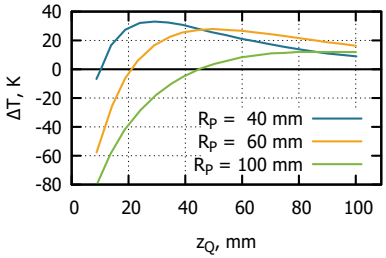

(b) The difference between center and rim temperatures Δt for different pedestal radii

Figure 3.11. Simplified temperature field simulation results from *FEMM* program, plotted over the heating region position z_Q.

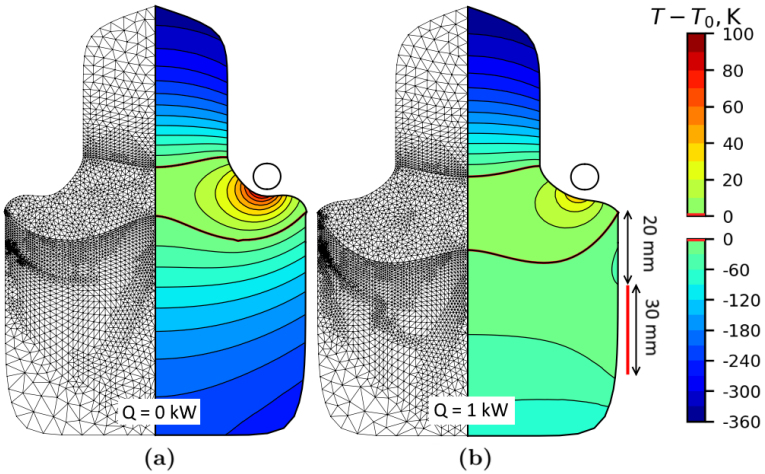

Figure 3.12. Mesh and silicon temperature, obtained with simplistically described side heating $Q = 0$ (a) and $Q = 1$ kW (b). Crystal diameter $D_C = 36$ mm and pedestal diameter $D_P = 75$ mm.

Larger melt height stabilized the system and allowed to use larger initial optimization step, than was previously used without the side heating (2 mm instead of 0.3 mm), and therefore to cover larger range of inductor parameter space, see Fig. 3.13. As a result, melt height was increased to $H_M = 25.2$ mm – twice higher than in the previous simulations without the side heating.

It should be noticed that the selection of the initial inductor shape has been done manually – by computing the shape of phase boundaries for multiple inductor shapes. Many of them diverged, especially for larger crystal diameters, which are described in the next section. The best performing shape was then selected and used as an initial shape in the gradient method. This is the reason why initial shapes are not the same in different figures, and the influence of initial conditions is discussed in the next section.

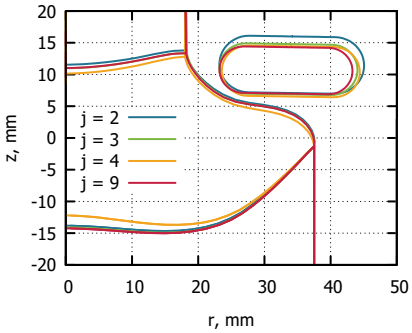

(a) Phase boundaries

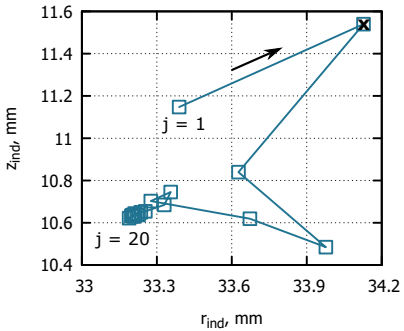

(b) Inductor cross-section center coordinates r_{ind} un z_{ind}

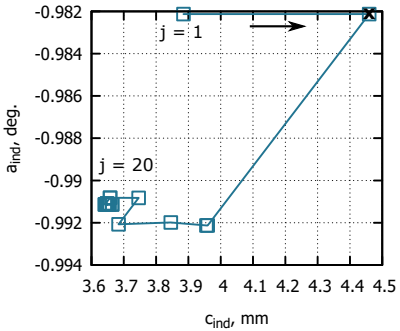

(c) Inductor cross-section inclination angle α_{ind} and curvature radius c_{ind}

Figure 3.13. The convergence of phase boundaries (a) and inductor parameters (b, c) during the optimization with gradient method, for different iteration numbers j. Simplified side heating $Q = 1$ kW. Diverged calculations are marked with $\times$.

3.4 Full system: side heating with middle-frequency inductor

In the present section, simulation results for different crystal and pedestal diameters are described. The crystal was pulled with a rate of 2 mm/min. Due to the advances of experimental system, simulation setup was refined by adding the copper shield and the precise shape of middle-frequency (MF) inductor, see Fig. 3.14. The main system parameters are given in Tab. 3.2. In the following subsections, the results of inductor optimization for crystal diameters 36, 60 and 100 mm.

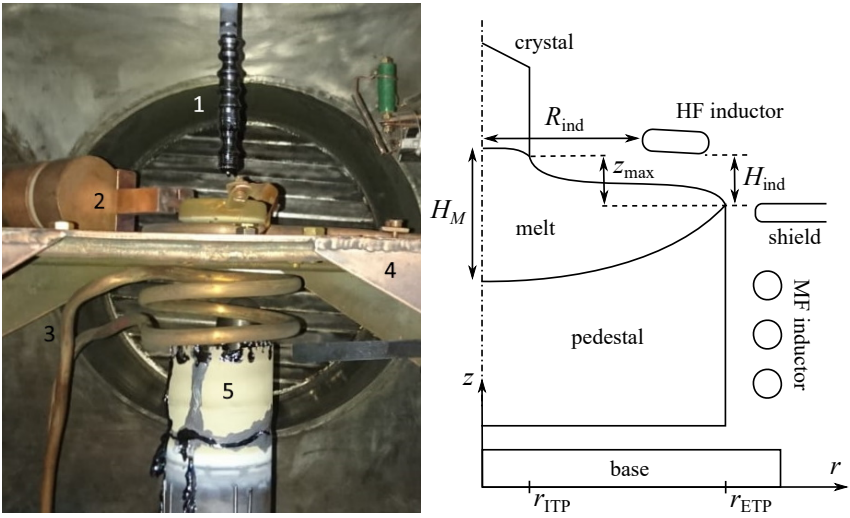

(a) Photograph of the growth chamber **(b)** Pedestal system scheme

Figure 3.14. A photograph of the growth apparatus (a) and the scheme of the system (b) with the grown irregular-shaped crystal sample 1, the high-frequency and middle-frequency inductors 2-3, copper shield 4 and the pedestal 5.

Crystal diameter of 36 mm

For the inductor optimization with 36 mm crystal, pedestal diameter was set to $D_P = 75$ mm. Relatively long initial inductor cross-section ($k_{\text{ind}} = 5$ mm) was selected in order to increase algorithm sensitivity on α_{ind}, as it was shown in the previous section. The gradient method converged at melt height $H_M = 24$ mm, see Fig. 3.15(a), where phase boundaries are shown at several iterations. H_M increased during the optimization, because HF EM heat was redistributed towards the melt center by changing inductor inclination angle α_{ind}. A similar trend was observed

Table 3.2. Summary of the used system parameters.

Crystal length	60 mm
Pedestal height	120 mm
HF inductor frequency f_{HF}	2.8 MHz,
Copper shield	
Gap between the shield and the pedestal	4 mm
Width of the shield rim	6 mm
Vertical position	$\sim$ ETP level
MF inductor	
Tube diameter	10 mm
Distance between windings	20 mm
Distance to the shield	15 mm
Distance to the pedestal side	9 mm
Frequency f_{MF}	100 kHz
Heating power Q_{MF}	depends on D_C, see Tab. 3.3

also when different initial geometry was tested ("thin" instead of "thick", see Fig. 3.15(b)).

The more detailed tracking of inductor parameters during the progress of gradient method is given in Fig. 3.16. It can be concluded that relatively large domain – several mm and almost 10°– of parameter space has been covered. After diverged simulations, the algorithm returned to the previous inductor geometry and halved the step length (as described in Sec. 2.5), which allowed to continue until the user-defined limit of 15 iterations. H_M value, however, was very close to the optimum already at the 4th iteration, see Fig. 3.16(d).

The final inductor shapes for different initial geometries were rather different, which means that the obtained final $H_M = 24$ mm may not be the global maximum. However, the final H_M values were close enough, therefore the optimization algorithm can be considered useful for a practical purpose: choosing an appropriate inductor in the future, for first experiments with larger D_C.

Crystal diameter of 60 mm

For the modelling of 60 mm crystal growth, $D_P = 150$ mm was selected, because in Section 3.1 the importance of $D_P \geq 2D_C$ criterion was

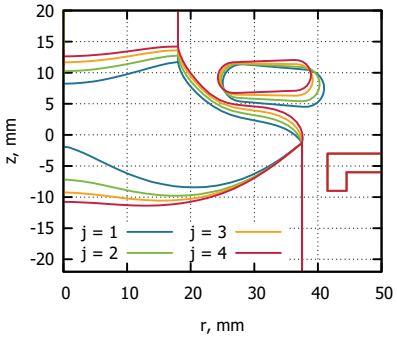

(a) Initial geometry Nr. 1: "thick" inductor

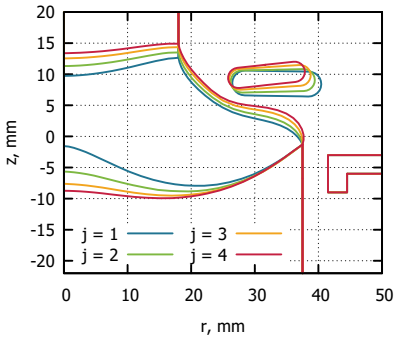

(b) Initial geometry Nr. 2: "thin" inductor

Figure 3.15. Examples of phase boundaries during the inductor optimization (j is iteration number), for different initial geometries.

demonstrated. In Fig. 3.17(a) the results of the previous, simplified side heating model, that was described in Sec. 3.3 is shown. Due to the imprecision of the simplified model (constant flux density instead of MF field simulations, the absence of the copper shield), calculations were unstable and optimization step size was reduced to prevent calculations from diverging. As a result, inductor changes were very small, and melt height H_M barely exceeded 20 mm. This unsuccessful optimization attempt is mentioned only for context, and the further text and Figures 3.17(b–d) consider only the results obtained with the actual middle-frequency EM field model, described in Section 2.2.

Optimization of all inductor parameters. Fig. 3.17(b) shows that the inductor shape substantially changes during the optimization, and the inclination α_{ind} of the cross-section increases – as well as in case with the 36 mm crystal. However, it should be noted that the stability of the numerical model decreased: to start the optimization algorithm, initial inductor shape, with which process modelling is at least possible, should be "guessed", and this guess was harder to make for larger D_C.

Optimization of all parameters except α_{ind}. The algorithm implementation makes it possible to exclude one or several inductor parameters from optimization. For example, Fig. 3.17(c) demonstrates the shape of phase boundaries during iterations with fixed α_{ind}. Optimal H_M value is,

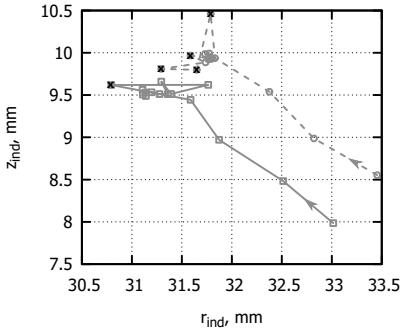

(a) Inductor cross-section center coordinates r_{ind} and z_{ind}

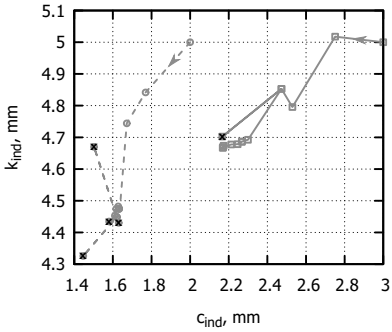

(b) Inductor cross-section curvature radius c_{ind} and length k_{ind}

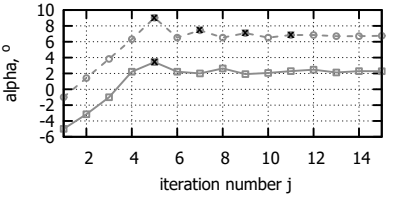

(c) Inductor cross-section inclination α_{ind}

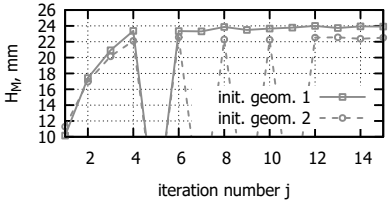

(d) Melt height H_M

Figure 3.16. The evolution of inductor slice parameters and melt height H_M during the inductor optimization for crystal diameter $D_C = 36$ mm and pedestal diameter $D_P = 75$ mm. Diverged calculations are marked with $\times$. Solid lines – "thick" initial inductor, dashed lines – "thin" initial inductor.

rather surprisingly, even larger than in the case of all parameter optimization, possibly due to the complicated shape of target function in the phase space: fixing one coordinate allows to bypass the closest local maximum.

Optimization of r_{ind} and z_{ind} only. For the convenience of inductor manufacturing, e.g., producing several inductors from the same copper tube, the reduced phase space – limited only to r_{ind} and z_{ind} – was tested. In this case, as shown in Fig. 3.17(d), optimization algorithm can suggest a solution with as large H_M as it was obtained by optimizing more inductor parameters. Therefore, particular inductor cross-section shape is not important, and only basic geometrical properties matter (more detailed analysis in Sec. 3.6.1).

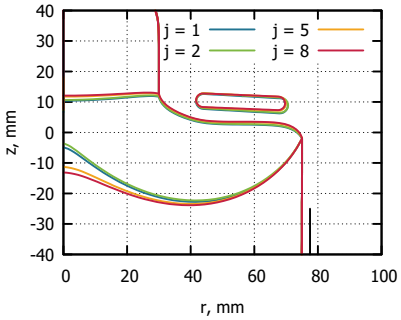

(a) Optimization of all inductor parameters, previously used simplified side heating.

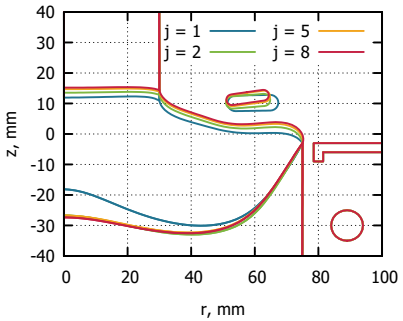

(b) Optimization of all inductor parameters, actual MF EM field model.

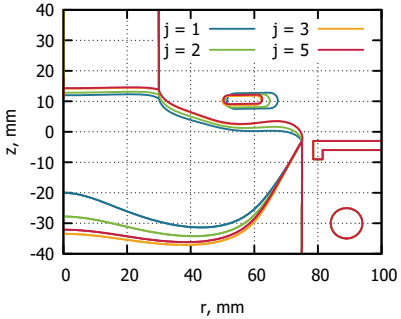

(c) Optimization of all parameters except α_{ind}, actual MF EM field model.

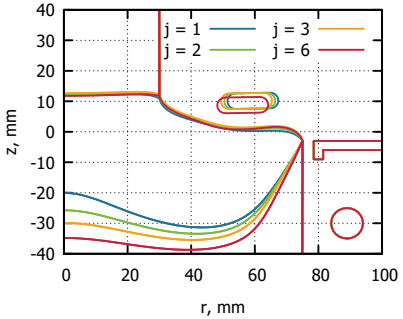

(d) Optimization of r_{ind} and z_{ind} only, actual MF EM field model.

Figure 3.17. Examples of phase boundaries during the inductor optimization (j is iteration number): crystal diameter $D_C = 60$ mm, pedestal diameter $D_P = 150$ mm.

Comparison of the optimization results. The optimized inductor shapes, as well as resulting phase boundaries, are shown in Fig. 3.18. At the left part, the results obtained from different initial conditions are shown, 36 mm crystal diameter was used. It can be concluded that the inductor shapes did not get closer to each other during the optimization – they are approximately as different as the initial shapes, shown in Fig. 3.15 with blue lines. In Fig. 3.18(b), the results of inductor optimization with different constraints are shown for the system with 60 mm crystal. The resulting shapes and positions are rather different, however the inductor height above the melt in the three considered cases is similar – 5.9, 6.2 and 5.2 mm, correspondingly.

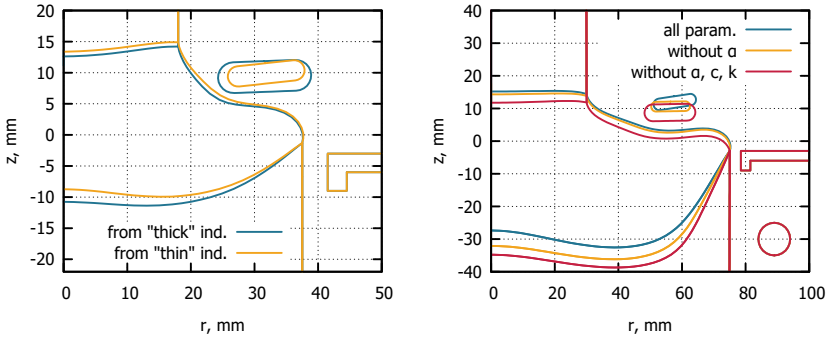

(a) $D_C = 36$ mm, $D_P = 75$ mm, different initial inductor shapes.

(b) $D_C = 60$ mm, $D_P = 150$ mm, different parameters excluded from optimization.

Figure 3.18. The optimized high-frequency inductor shape and the resulting phase boundaries. The (b) part shows also the cases, where some of the inductor parameters were not optimized: cross-section inclination angle α_{ind}, curvature radius c_{ind}, cross-section length k_{ind}.

Crystal diameter of 100 mm

For such large crystal and pedestal ($D_P = 200$ mm), it was very hard to find an appropriate initial shape of the inductor. Moreover, the optimization step must be very small ($s = 0.4$ mm in the simulations that are described below) due to high sensitivity of the system. Thus the overall change of inductor shape during the optimization was minuscule, see Fig. 3.19(a). Number of diverged calculations is larger, and the size of considered phase space region is much smaller, than for smaller D_C, see Fig. 3.19(b). The optimal inductor parameters are very close to the parameters of the diverged cases, where the melt spilled over the ETP due to large meniscus angle.

Target function modification

The problem of melt spilling was addressed by modifying target function of the optimization algorithm to include meniscus angle α_{ETP} (the angle between the free surface at the ETP and z axis, defined in Fig. 3.20):

$$f_t(H_M, \alpha_{\mathrm{ETP}}) = \begin{cases} H_M, & \text{for } \alpha_{\mathrm{ETP}} < 0 \\ H_M \cdot \left(1 - \dfrac{\alpha_{\mathrm{ETP}}}{30^\circ}\right), & \text{for } \alpha_{\mathrm{ETP}} > 0 \end{cases} \tag{3.6}$$

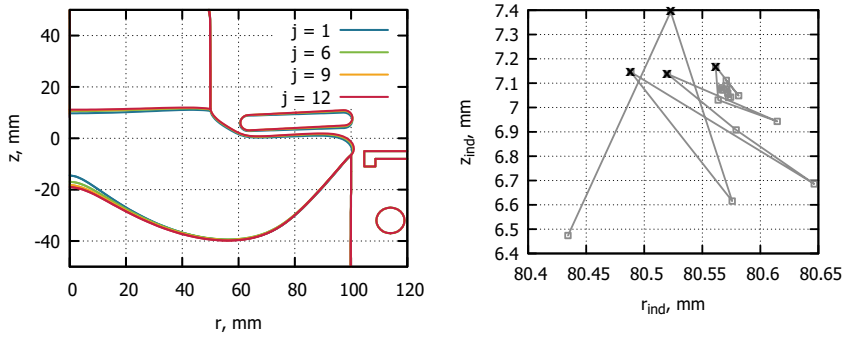

(a) Phase boundaries **(b)** Inductor slice center coordinates

Figure 3.19. Examples of phase boundaries (a) and the evolution of inductor cross-section center coordinates (b) during the inductor optimization with crystal diameter $D_C = 100$ mm and pedestal diameter $D_P = 200$ mm. Diverged calculations are marked with $\times$; j is the iteration number.

The usage of this formula increased the simulation stability and decreased the number of diverged cases. The optimization results for 100 mm crystal are shown in Fig. 3.20(a). Unlike the previous target function, with the modified target function H_M slightly decreased during the optimization. The reason is that f_t increase is now strongly determined by the decrease of α_{ETP}, see Fig. 3.21(a); and that the decrease of α_{ETP} usually means the redistribution of EM field away from the melt center, which decreases H_M. When H_M is large enough, its minor decrease is not a problem, because the process stability is in this case more dependent on α_{ETP} – preventing melt spilling over the pedestal rim.

The considered inductor parameters for 100 mm crystal growth, although converging, were still constrained to a very small range, as shown in Fig. 3.21(b). However, the inductor optimization for the smaller crystal growth ($D_C = 60$ mm) produced large changes in the inductor shape, that successfully increased H_M while keeping α_{ETP} small enough, see Fig. 3.20(b).

3.5 Model verification

Experimental data. The system parameters that were used for the model verification are the same as mentioned in Tab. 3.2 with the exception of $f_{\mathrm{HF}} = 2.64\,\mathrm{MHz}$. The growth chamber has been developed using

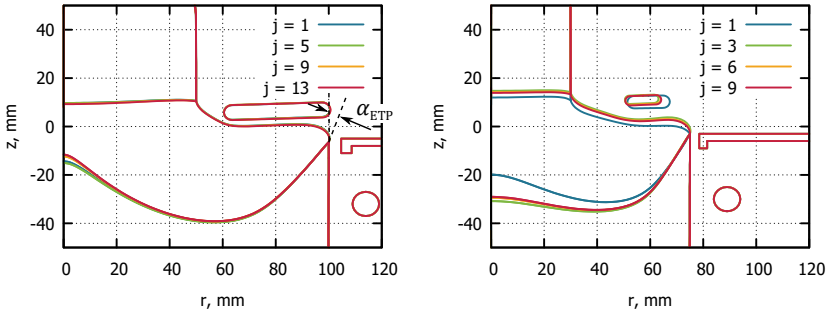

(a) $D_C = 100$ mm, $D_P = 200$ mm **(b)** $D_C = 60$ mm, $D_P = 150$ mm

Figure 3.20. Examples of phase boundaries during the inductor optimization with modified target function $f_t(H_M, \alpha_{\mathrm{ETP}})$, with different crystal and pedestal diameters D_C and D_P. H_M is the melt height, α_{ETP} is the angle between the free surface and vertical at the ETP.

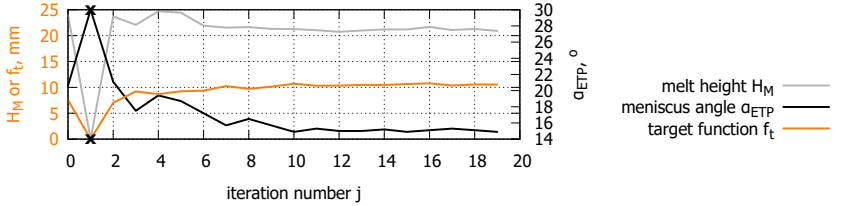

(a) Melt height H_M, meniscus angle α_{ETP} and target function $f_t(H_M, \alpha_{\mathrm{ETP}})$

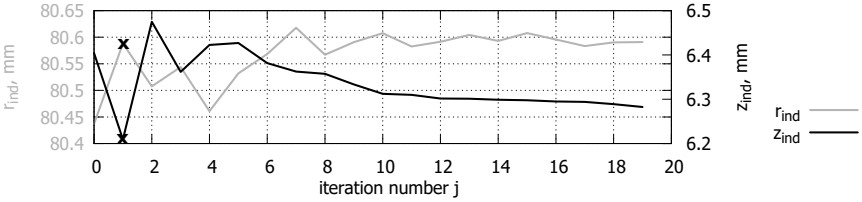

(b) Inductor cross-section center coordinates r_{ind} and z_{ind}

Figure 3.21. The evolution of target function components and inductor parameters during the optimization, with crystal diameter $D_C = 100$ mm and pedestal diameter $D_P = 200$ mm. Diverged simulations are marked with $\times$.

a vacuum furnace, that previously hosted another Si growth process at *KEPP EU* company: a modification of Czochralski process, where the heating was realized using an electron beam. The growth apparatus is de-

scribed in [Dis5] in more details. A pedestal with diameter $D_P = 75$ mm, produced with the electron beam method, was used. Unfortunately, the process was not stable enough to obtain a single crystal, and only polycrystalline rods were grown. A typical example is shown in Fig. 3.22, with diameter varying from 15 mm to 20 mm. Other polycrystalline rods were pulled with diameters from 9 to 22 mm, while diameter oscillation magnitude was limited to 3 mm in the most stable cases. The oscillations of the rod diameter may be explained by non-optimal HF inductor power control during the experiment.

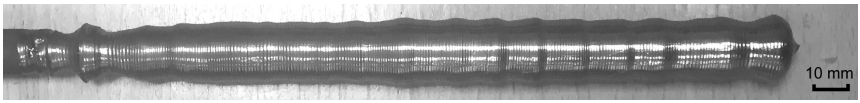

Figure 3.22. Polycrystalline sample with varying diameter that was grown from a pedestal with diameter of 75 mm.

Simulation results. Numerical modelling of the described system was also challenging because of melt center freezing. A reasonable melt shape was obtained with $Q_{\mathrm{MF}} = 1.6$ kW and $Q_{\mathrm{HF}} = 2.2$ kW (see Fig. 3.23, where T_0 denotes silicon melting temperature). There are no available recordings of corresponding power values during the experiment.

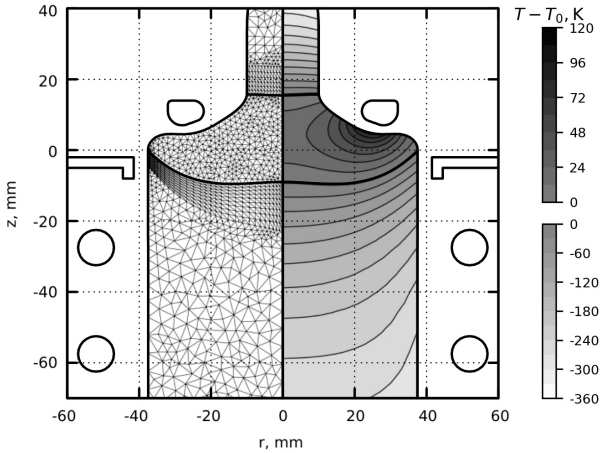

Figure 3.23. An example of finite element mesh (left) and calculated temperature field (right) for the system with crystal diameter $D_C = 20$ mm and pedestal diameter $D_P = 75$ mm.

After the growth of polycrystalline rod, shown in Fig. 3.22, the remaining pedestal was cut and the melting interface shape was detected by bond decoration etching with potassium hydroxide, see Fig. 3.24(a). This experimentally obtained profile is compared to the simulation result in Fig. 3.24(b). Correspondence to the experiment was slightly improved when the distance between the middle-frequency coil and the shield Δz_{MF} was increased. This mismatch could be explained by non-symmetrical experimental coil – as the tube bends downwards in actual 3D shape, appropriate value of Δz_{MF} for axially symmetrical model decreases.

There were no Si growth experiments found in the literature that correspond to the system modelled in this work. However, in another system [46], where an electron gun was used instead of a high-frequency inductor, and the crystal was positioned asymmetrically with respect to the pedestal, a qualitatively similar shape of the melting front was observed: with a double curvature, see Fig. 3.25.

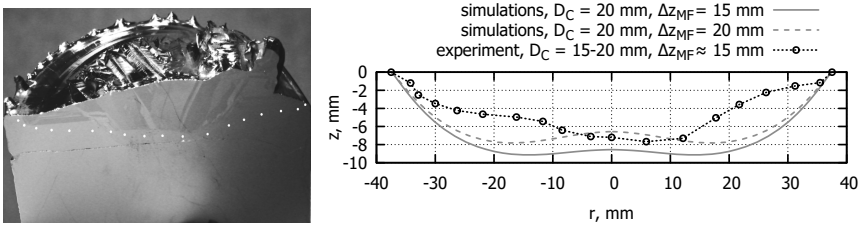

(a) Vertical slice of the pedestal **(b)** Comparison between simulated and experimentally measured melting front shapes

Figure 3.24. Experimentally measured (a) and simulated (b) melting front shapes for the system with crystal diameter $D_C = 20$ mm, pedestal diameter $D_P = 75$ mm. Δz_{MF} is the distance between the middle-frequency coil and the shield.

Discussion. Even after the coil height correction, calculated interface shape only qualitatively corresponds to the experimental one, with differences up to 4 mm. It can occur due to multiple reasons: unsteadiness of the experiment, non-horizontal ETP line, other imprecisions of experimental set-up, non-symmetry of the experimental inductor due to power supply circuits, and the lack of melt flow in the model.

The effect of the non-symmetry of the HF inductor could manifest as lower induced heat below the gap between current suppliers, which decreases melting interface depth. It could explain why the experimental

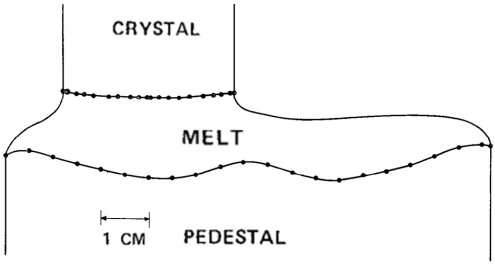

Figure 3.25. Experimentally measured melting and crystallization front shapes in the system with electron gun and asymmetrically positioned crystal [46].

interface in Fig. 3.24(b) is shallower at the right side ($r > 0$). If evaluated by analyzing a research where the main slit width was changed in FZ system [68], this effect is unlikely to exceed 1 mm. However, unlike the FZ crystal, the pedestal did not rotate in the considered experiment, therefore larger non-symmetrical effects could be expected. The imprecisions of experimentally measured interface are hard to analyze because of the non-symmetry and the lack of statistics.

The melt flow effect has been previously investigated in a simplified system (see Sec. 3.2.2 or [Dis4]), and rather should increase interface deflection at $r \approx 25$ mm due to the vortex created by HF EM force. However, that research did not include MF EM force, which acts in the direction away from the melting interface. Thus, MF EM force should decrease interface depth at the outer part of the interface and improve the fitting to the experiment. The order of magnitude of the melt flow influence on a FZ system with similar proportions ($D_C = 100$ mm) was predicted to be several millimeters large [69].

Simulations of melt flow. The middle-frequency EM field simulations, described in Sec. 2.2, allowed to obtain time-averaged Lorentz force density in melt:

$$f_{\mathrm{MF}} = 0.5\vec{j} \times \vec{B},$$

where $\vec{j}$ is the magnitude of induced current density and $\vec{B}$ is the magnitude of magnetic field. The obtained force density distribution is shown in Fig. 3.26. The force is indeed directed away from the interface and has a maximum at moderately large r. However, the melt flow calculations with *OpenFOAM*, the model of which is described in Sec. 2.4, show that the influence of MF volume force is very small in comparison with the surface

force induced by the HF inductor. The two-vortex structure of melt flow, shown in Fig. 3.27, remains the same, and brings hot silicon from the free surface towards the melting interface. The Figure depicts the whole velocity – azimuthal component of it is very small, because crystal and pedestal were not rotating

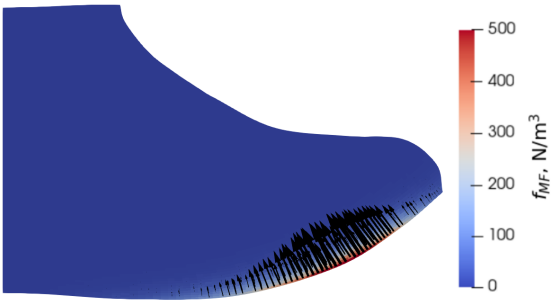

Figure 3.26. The time-averaged Lorentz force volume density f_{MF} induced in melt by the MF coil in the system with crystal diameter $D_C = 20$ mm and pedestal diameter $D_P = 75$ mm.

To evaluate the influence of melt flow on the shape of the melting interface, heat flux correction was introduced. It was defined as the difference between the heat fluxes calculated with and without melt flow: $q_{\mathrm{corr}} = q_{\mathrm{melt\ flow}} - q_{\mathrm{no\ melt\ flow}}$. Using this definition, positive values of q_{corr} would mean additional crystallization (i.e., the interface shifts upwards), negative values – melting (the interface shifts downwards). In all considered cases, q_{corr} is mostly negative, see Fig. 3.28. It means that the simulated interface shape cannot be moved closer to the experimental shape using f_{MF}. The same conclusion applies for 2.3 times finer mesh, and even when f_{MF} was scaled twice, it was still neglectable in comparison with HF induced force.

Model limitations. One of the main limitations of the numerical model is that it uses the axially symmetric approximation. In the experimental system, the HF inductor is highly asymmetric: it consists of a single loop and there is a gap between its suppliers. Most of the melt flow calculations were also performed in the axially symmetric approximation.

The second important constraint is that the model is quasi-stationary. It describes the phase boundaries and the melt flow at equilibrium, which is established for given boundary conditions. Therefore, if the experiments

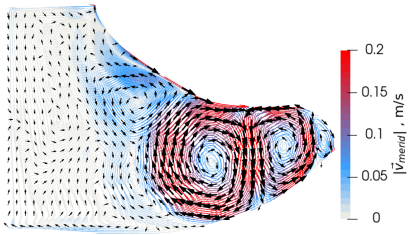

(a) Meridional (projected on a vertical plane) melt velocity without MF force.

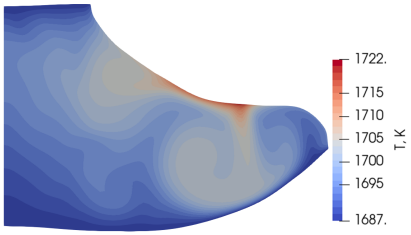

(b) Melt temperature without MF force.

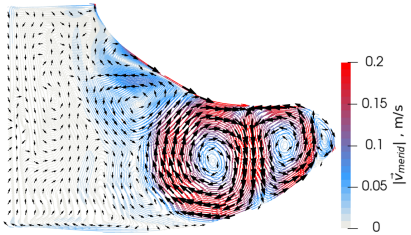

(c) Meridional (projected on a vertical plane) melt velocity with MF force.

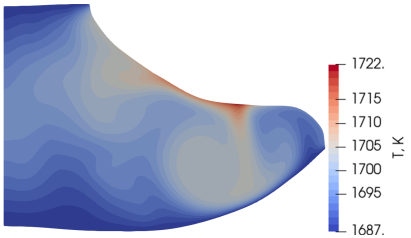

(d) Melt temperature with MF force.

Figure 3.27. The results of melt flow calculations without (top) and with (bottom) the force induced by the middle-frequency inductor; $D_C = 20$ mm, $D_P = 75$ mm.

were carried out in a non-equilibrium state (e.g. if the melting front was changing during the experiment), they are more difficult to use for model verification. Another limitation is that only laminar flow is considered. However, the resulting vortex structure is rather stable and distinct, so the effect of melt flow on heat transfer would not change significantly if a turbulence model were used.

Despite the differences between the experiment and simulation results, numerical investigation about the crystal diameter increase and optimal inductor shapes are valuable to understand approximate values of optimal inductor parameters and their dependence on crystal diameter.

3.6 Challenges of large diameter crystal growth

3.6.1 Optimized shapes of high-frequency inductor

The summary of optimal inductor parameters for different crystal and pedestal diameters is shown in Tab. 3.3. Middle-frequency inductor power

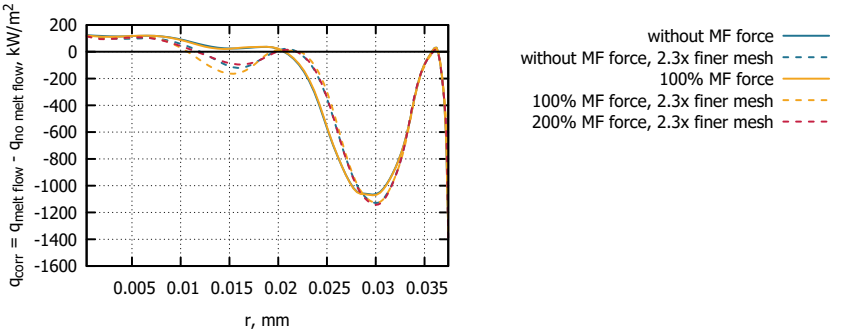

Figure 3.28. The heat flux correction q_{corr} on the melting interface, calculated as heat flux difference between simulations with and without melt flow.

Q_{MF} has not been optimized in the present research: Q_{MF} has been manually selected for each pedestal to ensure calculation convergence with initial HF inductor geometry and kept constant during all iterations. Exclusion of some parameters from optimization algorithm has rather small influence on the results: 1-3 mm difference in H_M is not crucial for the preventing of melt center freezing, and it is also small in the context of the discrepancy between the experiment and the simulations. Moreover, the required HF and MF power values are practically the same regardless of inductor shape. These results indicate that the remaining degrees of freedom of the inductor shape may be used in the future to optimize other process aspects, that have not been optimized yet (e.g. melt flow intensity or HF inductor voltage).

Fig. 3.29 shows a visual representation of several columns of Tab. 3.3. As it follows from the pedestal method design, internal diameter of the inductor D_{ind} increases for larger D_C. However, this increase is not linear, and the difference between D_{ind} and D_C is the largest for $D_C = 60$ mm: almost 40 mm, or one third of crystal diameter. For now it is not clear whether this behavior can be attributed to the selection of initial inductor parameters (and in the system with 100 mm crystal the inductor shape is far from optimal) or can be considered a feature of the pedestal method itself. Fig. 3.29(a), also shows that the optimal distance H_{ind} between the inductor and the ETP is ~ 10 mm independently of D_C.

Necessary induced HF inductor power is higher than MF inductor power (pedestal side heating) in cases with large D_C, see Fig. 3.29(b). It outlines a challenge connected with crystal diameter increase: higher

HF inductor current increases the risk of arc discharge and intensifies melt convection, thus destabilizing free surface and melting interface shapes. Finally, the process stability could also be an important issue: when Fig. 3.19 and Fig. 3.15 are compared, the range of possible inductor shapes is much smaller in the case with the larger D_C. It demands the precision of the inductor manufacturing and growth process control. Possibly, the inclusion of MF inductor parameter (current, frequency, distance between windings) in the optimization algorithm could improve the stability of the molten zone and decrease necessary HF inductor power.

Fig. 3.30 shows that in almost all inductor optimization simulations, zone height $z_{\max}$ is 1–2 mm higher than the one calculated using Laplace-Young equation in Section 3.1. It demonstrates the stabilizing effect of EM pressure, as described in [66].

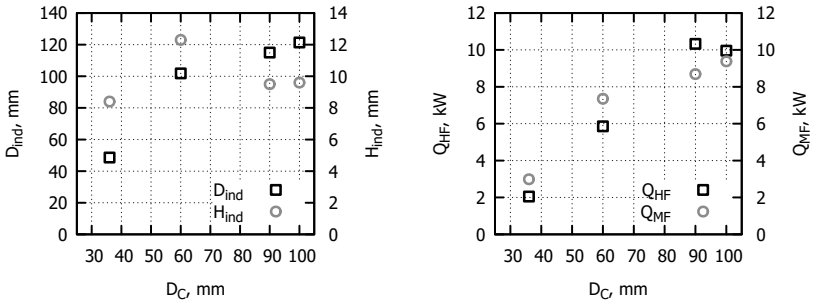

(a) Internal diameter of the inductor D_{ind} and height above the ETP H_{ind}

(b) Necessary high-frequency EM and middle-frequency EM induced power

Figure 3.29. Summary of inductor optimization results: inductor parameters and heating power values, plotted over the crystal diameter D_C.

Table 3.3. Summary of inductor optimization results and used EM power for crystal and pedestal diameters D_C and D_P. The "without" keyword indicates which HF inductor parameters were excluded from the optimization. R_{ind} is the internal radius of the high-frequency inductor, H_{ind} – inductor height above the pedestal rim, H_M – melt height, $z_{\max}$ – the vertical distance between the ITP and the ETP, Q_{HF} and Q_{MF} – the integral powers of high-frequency and middle-frequency inductor. Target function is denoted by f_t.

D_C; D_P, mm	case details	R_{ind}, mm	H_{ind}	H_M, mm	$z_{\max}$, mm	Q_{HF}, kW	Q_{MF}, kW
36; 75	"thick" initial geometry	24	8.4	24	15.8	2.1	3.0
	"thin" initial geometry	26	9.1	22	16.2	2.1	3.0
60; 150	–	51	12.3	45	17.3	5.9	7.3
	without α_{ind}	50	12.1	46	16.9	5.9	7.3
	without $c_{\text{ind}}, k_{\text{ind}}, \alpha_{\text{ind}}$	49	9.7	45	15.1	5.8	7.3
	modified $f_t(H_M, \alpha_{\text{ETP}})$	51	11.8	43	16.4	5.8	7.3
90; 200	–	58	9.5	46	17.9	10.3	8.7
	without $c_{\text{ind}}, k_{\text{ind}}, \alpha_{\text{ind}}$	56	9.5	45	17.6	10.2	8.7
100; 200	–	61	9.6	30	17.9	10.0	9.4
	without $c_{\text{ind}}, k_{\text{ind}}, \alpha_{\text{ind}}$	60	9.5	27	17.5	9.9	9.4
	modified $f_t(H_M, \alpha_{\text{ETP}})$	61	9.2	21	16.9	9.8	9.5

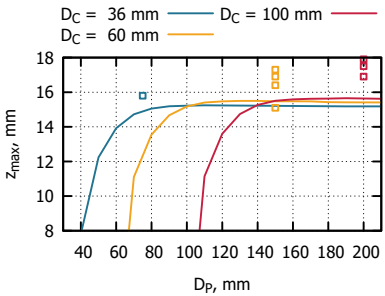

Figure 3.30. Maximal zone height $z_{\max}$ for different crystal diameters D_C and pedestal diameters D_P, obtained by Laplace-Young equation (lines) and in inductor optimization simulations (points).

3.6.2 Additional free surface heating during the cone phase

The previous section presented the results of inductor shape optimization for different crystal diameters D_C. However, it is impossible to change the inductor during the growth process. It means that the initial pedestal melting, crystal seeding and start cone phase (gradual increase of D_C) must be performed with the same HF inductor. The inductor that was optimized for large D_C, and thus has large inner diameter, is clearly suboptimal for small crystal growth, because it does not induce enough heat in the pedestal center to compensate large heat losses from the central part. This effect was also shown in experiments even with relatively small pedestal of $D_P = 75$ mm, see Fig. 3.31(a). This problem can be mitigated by using a third source of heat that helps to sustain large temperature at the pedestal center, e.g. infrared lamps, schematically shown in Fig. 3.31(b).

Simulations of phase boundaries. The present section describes the calculations of phase boundaries for $D_P = 200$ mm and different crystal diameters (from 10 to 100 mm), performed to find appropriate proportions of HF, MF and additional free surface (FS) heating during the cone growth. Other system parameters correspond to Tab. 3.2.

During the study, inductor shape remained constant, and inductor current was adjusted using a PID algorithm to keep vertical distance to the ETP constant: $H_{\text{ind}} = 9$ mm (see Fig. 3.31(b)) for all of considered D_C. In this way, total induced HF heat Q_{HF} has been obtained for each calculation. Other integral heat fluxes were user-defined. Q_{FS} was defined

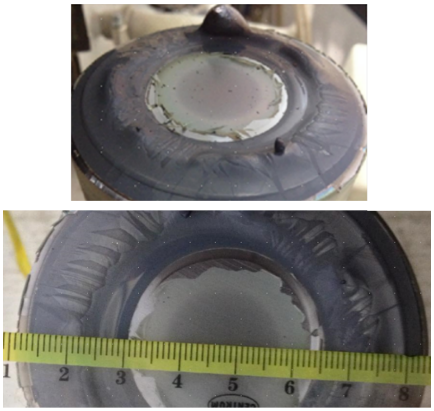

(a) Pedestal surface photographs after unsuccessful attempts to melt it without additional heat source on the free surface

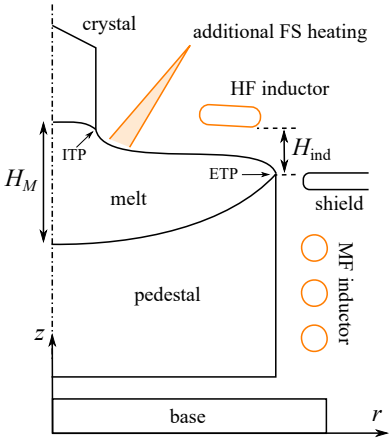

(b) System scheme, where heat sources are shown in orange, including the additional free surface (FS) heating

Figure 3.31. Pedestal ($D_P = 75$ mm) surface photographs and the scheme of the modelled system.

directly, Q_{MF} was defined indirectly – by defining MF inductor current. Multiple values were tested, and only some of calculations converged. For example, melt center was freezing when Q_{MF} was set too low, and part of FS crystallized near the internal triple point (ITP) if Q_{FS} was set too low. In this section, the calculations with the lowest possible values of additional heat fluxes Q_{FS} and Q_{MF} are summarized, as they are beneficial for cost-effectiveness and equipment design.

The optimal integral heat fluxes during the cone phase are given in Fig. 3.32, indicating that the free surface heating should be gradually decreased, and for $D_C > 60$ mm MF heating should start to increase. Corresponding phase boundaries and silicon temperature distributions are presented in Fig. 3.33. Both H_M value and FS meniscus angle are satisfactory, i.e. do not threaten stable growth process, for all of crystal diameters. However, H_M is only 21 mm in $D_C = 100$ mm system, which means that further increase of D_C may not be possible with current pedestal diameter $D_P = 200$ mm.

Fig. 3.34 demonstrates the influence of pedestal diameter increase on phase boundaries. It stabilizes the process by increasing H_M and de-

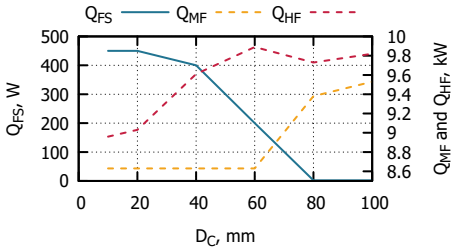

Figure 3.32. The optimal values of integral free surface heat Q_{FS}, middle-frequency induced heat Q_{MF} and high-frequency induced heat Q_{HF} during the cone phase (modelled by quasi-stationary simulations with different crystal diameters D_C).

creasing α_{ETP}, however it has its drawbacks: harder manufacturing of the pedestal and larger heat losses, that lead to almost 50% increase in required HF inductor power. The increase of necessary HF power also puts additional requirements on EM generator.

Figure 3.35 demonstrates the influence of Q_{FS} on phase boundaries, while $D_C = 10$ mm and other parameters are constant. The embedded graph shows also the molten zone height $z_{\max}$, defined as vertical distance between the ETP and the ITP. Higher free surface heating increases zone height and melt height H_M, because melt temperature should drop for crystallization to happen, and it happens at higher z for higher Q_{FS}.

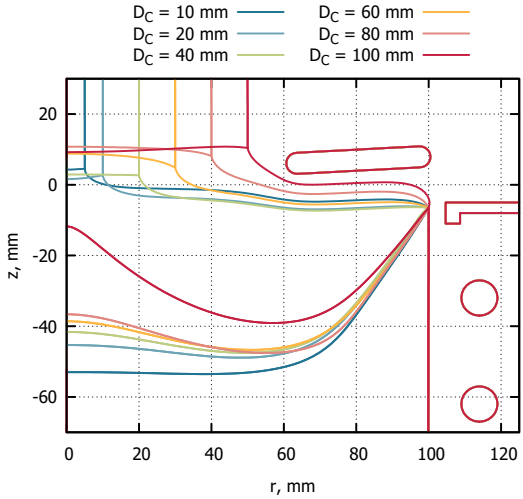

(a) Phase boundaries

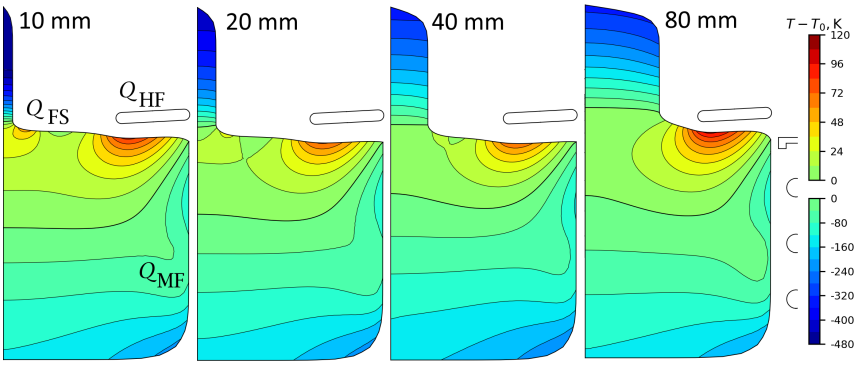

(b) Si temperature distributions, with heating region Q designations in the left image

Figure 3.33. Phase boundaries and Si temperature in the simulations with different crystal diameters D_C.

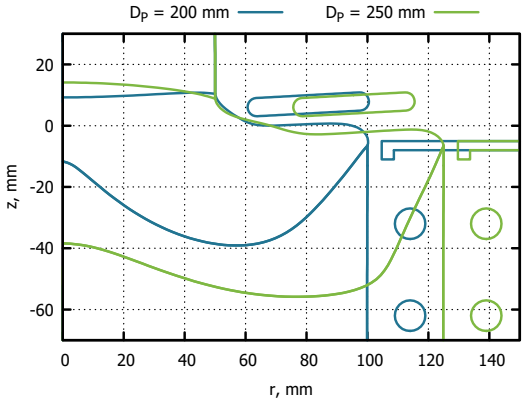

Figure 3.34. Shapes of phase boundaries with crystal diameter $D_C = 100$ mm and different pedestal diameters D_P.

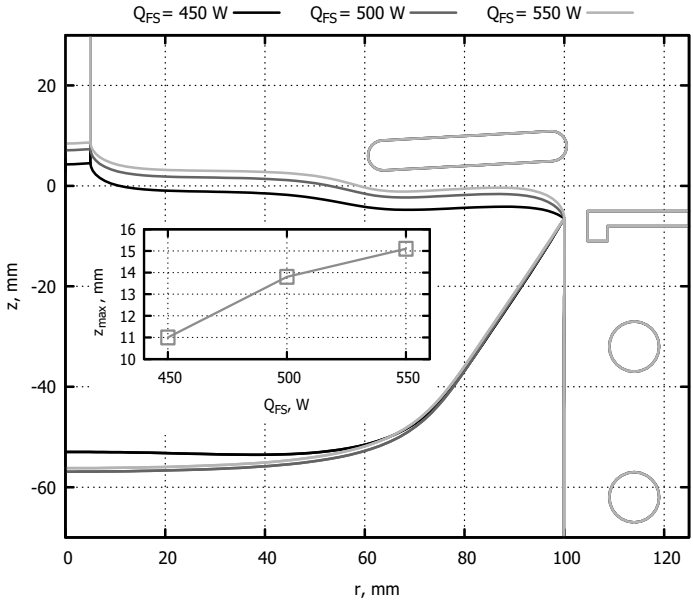

Figure 3.35. Shapes of phase boundaries and zone height $z_{\max}$ with crystal diameter $D_C = 10$ mm and different values of free surface heating power.

Analytical estimations of irradiated heat. If a crystal is sufficiently tall and thin, radial temperature gradient can be neglected, and the temperature in the crystal can be described using 1D distribution $T(z)$, see Fig. 3.36(a). As the crystal side surface is located far from the inductor, it can be assumed that the only source of temperature change is radiation. The dimensionless heat transport equation then becomes [69]:

$$\frac{\partial^2 \tilde{T}}{\partial \tilde{z}^2} = \tilde{q}_{\text{rad}} = \text{Bi}\,\tilde{T}^4, \qquad \text{Bi} = \frac{\varepsilon_s \sigma_{\text{SB}} T_0^3 R_C}{\lambda}, \tag{3.7}$$

where T_0 is melting temperature, $\tilde{T} = T/T_0$ is dimensionless temperature, $\tilde{z} = z/R_C$ is dimensionless vertical coordinate, $\tilde{q}_{\text{rad}}$ is dimensionless heat flux through the crystal side surface, Bi is Biot number, $\varepsilon_s = 0.46$ is solid silicon emissivity, $\sigma_{\text{SB}} = 5.67\,\text{W/m}^2\text{K}^4$ is Stefan-Boltzmann constant, and R_C is crystal radius. The boundary conditions for this problem are $\tilde{T}\Big|_{z=0} = 1$ at the crystallization interface and $\left.\dfrac{\partial \tilde{T}}{\partial z}\right|_{z=\infty} = 0$ far from the interface. The solution to the previous equation is

$$T(\tilde{z}) = \left(1 + \tilde{z}\sqrt{\frac{9}{5}\text{Bi}}\right)^{-\frac{2}{3}}, \tag{3.8}$$

which leads to dimensionless heat flux at the crystallization interface $\tilde{q}_{\text{crys}} = \dfrac{\partial \tilde{T}}{\partial \tilde{z}} = \sqrt{\dfrac{4}{5}\text{Bi}}$.

Therefore, the dimensional integral heat flux is

$$Q_{\text{crys}} = \tilde{q}_{\text{crys}} \cdot \frac{\pi R_C^2 \lambda T_0}{R_C} = \sqrt{\frac{4}{5}\text{Bi}} \cdot \pi R_C \lambda T_0. \tag{3.9}$$

The analytically obtained Q_{crys} is plotted in Fig. 3.36(b), with solid blue line. It partially corresponds to the simulation results, shown with the dashed blue line. Differences probably arise due to the increase of crystal radius, which makes the 1D approximation less precise, because the crystal length has been kept constant. Another possible explanation is the change of emissivity with temperature.

One could also try to analytically estimate heat losses from the free surface as $Q_{\text{free surf.}} \sim \varepsilon_l \sigma_{\text{SB}} T_0^4 \cdot \pi(R_P^2 - R_C^2)$ (uniform radiation from an area equal to the difference between pedestal and crystal cross-section areas, where liquid silicon emissivity $\varepsilon_l = 0.27$). However, this simplification

does not consider neither the presence of HF inductor nor the change of the melt surface shape, therefore it is not useful for systems with large D_C, as shown in Fig. 3.36 with gray lines. It means that the analytical estimations are not precise enough to predict the system behavior during the increase of D_C, and numerical simulations are important for experiment planning and realization.

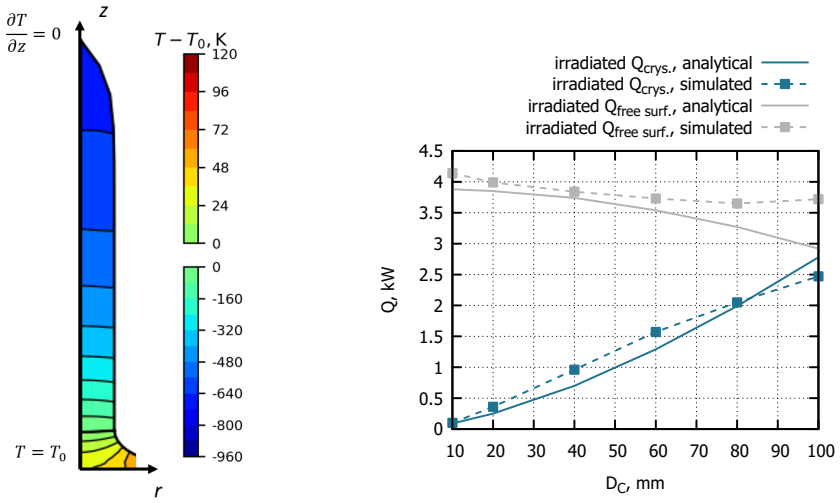

(a) **(b)**

Figure 3.36. (a) – temperature field in the crystal with radius $D_C = 10$ mm, that justifies the 1D approximation $T(z)$. (b) – comparison between analytical and numerically simulated total irradiated heat from the crystal side surface Q_{crys} and the melt free surface $Q_{\text{free surf.}}$.

4 Conclusions

In this work, the phase boundaries and melt flow during the growth of silicon crystals by the pedestal method are numerically modelled for the first time. The conclusions of the work are presented below, summarized according to the goal and the tasks of the work defined in the subsection 1.5. **The tasks** of the thesis have been completed:

1. The software for the modelling of pedestal method has been developed based on the floating zone method modelling software. The main program includes modelling of the electromagnetic field and the shape of the phase boundaries, while melt flow calculations have also been performed for some cases.

2. In line with the development of the experimental set-up at *KEPP EU*, the modelling software has also been improved: first by adding pedestal side heating in a simplified way (as homogeneous heat flow on the surface), and then by creating a more accurate middle-frequency field model.

3. Verification of the program by comparison with available experimental data has been carried out. This task was only partially completed as experimental data was only available from one growth process. This prevents a conclusion as to whether differences of up to 4 mm between the experimentally measured and numerically simulated melting front shape are significant in comparison with the uncertainty of the experimental data.

4. The optimization algorithm has been developed and used to adjust the shape of the high frequency inductor using the gradient method and to improve the melt height for different crystal diameters. The modelling resulted in optimal inductor parameters for crystals with diameters of 36, 60, 90 and 100 mm.

The goal of the work has been achieved: numerical models have shown that it is possible to grow silicon crystals with a diameter of 100 mm using the pedestal method. This is possible if pedestal side heating and additional free surface heating are used. In the framework of ERDF projects, the industrial partners *KEPP EU* regularly considered the simulation results and used them for the experiment design. During the projects, the

crystals grown by the industrial partners reached a diameter of 35 mm, which is approaching the limits found in the literature.

Thesis: simulation results confirm that it is possible to grow large (100 mm diameter) silicon crystals if improvements are made to the pedestal process. The main problems are freezing of the melt center and spilling of the melt as the free surface overhangs the edge of the pedestal. The necessary improvements are heating of the pedestal side with a middle-frequency inductor and additional heating of the free surface at the beginning of the cone phase. This statement is supported by a series of calculations. The high frequency inductor optimization algorithm, which takes into account both the melt height and the melt meniscus angle, allowed to obtain a stable molten zone for growing 100 mm crystals from a 200 mm pedestal. To further improve the stability of the zone, the diameter of the pedestal should be increased, e.g., to 250 mm.

The analysis of the results of the work also led to other conclusions:

- The calculations showed that high frequencies are more favorable for experiments, because the inductor current is lower and the melt motion is less intense.
- Calculations of melt flow using the volume-of-fluid method showed that a significantly deeper melt front is obtained when melt convection is taken into account.
- The inductor optimization calculations predict that the inductor should be horizontal or with a slight inclination "inwards", positioned approximately 10 mm above the ETP, and its other parameters are summarized in Table 3.3. If some inductor parameters were kept constant, this did not significantly affect the optimization results.
- In order to improve the process stability and to make the growth of 100 mm crystals feasible, side heating of the pedestal is necessary. However, even side heating is not sufficient at the very beginning of the process and in the cone phase with small crystal diameters. Therefore, in the part of the cone phase when the crystal diameter is less than 60 mm, additional free surface heating (e.g. with infrared lamps) is necessary, with a maximum value of about 500 W.

5 References

Author's publications, i.e. references like [Dis2], are summarized in Sec. 1.7.

[1] P. Müller, "Press information from 03/09/2020," tech. rep., Siltronic AG, 2020.

[2] N. V. Abrosimov, A. Lüdge, H. Riemann, and W. Schröder, "Lateral Photovoltage Scanning (LPS) Method for the Visualization of the Solid-Liquid Interface of Si_1-xGe_x Single Crystals," *Journal of Crystal Growth*, vol. 237, no. 1, pp. 356–360, 2002.

[3] A. Lüdge, H. Riemann, B. Hallmann-Seiffert, A. Muiznieks, and F. Schulze, "Rotationless floating zone crystal growth," in *ECS Transactions*, ECS, 2006.

[4] G. Dhanaraj and K. Byrappa, "Crystal Growth Techniques and Characterization: An Overview," in *Springer Handbook of Crystal Growth* (G. Dhanaraj, K. Byrappa, V. V. Prasad, and M. Dudley, eds.), ch. 1, pp. 3–15, Springer-Verlag, 2010.

[5] I. Milisavljevic and Y. Wu, "Current Status of Solid-state Single Crystal Growth," *BMC Materials*, vol. 2, no. 2, 2018.

[6] T. Teubner, T. Boeck, and K. Schmidt, "Modelling of Solution Growth of Silicon from Small Indium Droplets – Homogeneous Nucleation," *Journal of Crystal Growth*, vol. 198, no. 1, pp. 425–429, 1999.

[7] M. E. Jones and D. W. Shaw, "Growth from the vapor," in *Changes of State* (N. B. Hannay, ed.), pp. 283–323, Springer US, 1975.

[8] Chemistry LibreTexts, "7.10: Semiconductor Grade Silicon." https://chem.libretexts. org/@go/page/212899, retrieved December 23, 2021.

[9] A. Franzosi, L. Giarda, and L. Pelosini, "Process of Deposition of Single Crystal Silicon Directly from the Vapour Phase," tech. rep., Commission of the European Communities, 2019.

[10] National Center for Biotechnology Information, "PubChem Compound Summary for CID 23953, Silane." https://pubchem.ncbi.nlm.nih.gov/compound/Silane, retrieved October 6, 2021.

[11] A. Daw, D. Pal, and M. Kowar, "Modelling of Epitaxial Growth Rate of Silicon by Vapour Phase Epitaxy," *Microelectronics Journal*, vol. 21, no. 5, pp. 29–39, 1990.

[12] National Institute of Standards and Technology, U.S. Department of Commerce, "NIST Chemistry WebBook, SRD 69, Silicon." https://webbook.nist.gov/cgi/inchi?ID=C7440213, retrieved October 15, 2021.

[13] H. J. Scheel, *Crystal Growth Technology*. John Wiley & Sons Ltd., 2003.

[14] M. Arzakantsyan, N. Ananyan, V. Gevorgyan, and J.-C. Chanteloup, "Growth of Large 90 mm Diameter Yb:YAG Single Crystals with Bagdasarov Method," *Opt. Mater. Express*, vol. 2, no. 9, pp. 1219–1225, 2012.

[15] P. S. Dutta, "Bulk Crystal Growth of Ternary III–V Semiconductors," in *Springer Handbook of Crystal Growth* (G. Dhanaraj, K. Byrappa, V. V. Prasad, and M. Dudley, eds.), ch. 10, pp. 281–321, Springer-Verlag, 2010.

[16] K. Kakimoto, "Czochralski Silicon Single Crystals for Semiconductor and Solar Cell Applications," in *Springer Handbook of Crystal Growth* (G. Dhanaraj, K. Byrappa, V. V. Prasad, and M. Dudley, eds.), ch. 8, pp. 231–241, Springer-Verlag, 2010.

[17] S. Meroli, "Czochralski Process vs Float Zone: Two Growth Techniques for Mono-crystalline Silicon." https://meroli.web.cern.ch/lecture_silicon_-floatzone_ czochralski.html, retrieved December 23, 2021.

[18] H. Riemann, N. V. Abrosimov, J. Fischer, and M. Renner, "Method and apparatus for producing single crystals composed of semiconductor material," in *European Patent Office*, 2011. https://patents.google.com/patent/EP2504470A1/en.

[19] K. Dadzis, R. Menzel, U. Juda, K. Irmscher, C. Kranert, M. Müller, M. Ehrl, R. Weingärtner, C. Reimann, N. Abrosimov, and H. Riemann, "Characterization of Silicon Crystals Grown from Melt in a Granulate Crucible," *Journal of Electronic Materials*, vol. 49, pp. 5120–5132, 2020.

[20] H. A. Dabkowska and A. B. Dabkowski, "Crystal Growth of Oxides by Optical Floating Zone Technique," in *Springer Handbook of Crystal Growth* (G. Dhanaraj, K. Byrappa, V. V. Prasad, and M. Dudley, eds.), ch. 12, pp. 367–386, Springer-Verlag, 2010.

[21] P. H. Keck and M. J. E. Golay, "Crystallization of Silicon from a Floating Liquid Zone," *Physical Review*, vol. 89, pp. 1297–1297, 1953.

[22] L. Altmannshofer, M. Grundner, J. Virbulis, and J. Hage, "A Material Innovation for the Electronic Industry: Float Zone Single Crystal Silicon With 200 mm Diameter," in *ISPSD'03. IEEE 15th International Symposium on Power Semiconductor Devices and ICs*, pp. 325–328, IEEE, 2003.

[23] W. C. Dash, "Silicon Crystals Free of Dislocations," *Journal of Applied Physics*, vol. 29, p. 736, 1958.

[24] A. Borghesi, M. Geddo, and G. Guizzetti, "Characterization of Impurities in Silicon by IR Spectroscopy," *Helvetica Physica Acta*, vol. 62, pp. 6–7, 1989.

[25] M. Wünscher, A. Ludge, and H. Riemann, "Crucible-free Crystal Growth of Silicon and Germanium – Numerical Simulation and Check by Experiments," in *Modelling for Electromagnetic Processing*, pp. 97–102, 2008.

[26] J. Bernreuter, "Solar-Grade Silicon: Expensive and in Short Supply," *Sun & Wind Energy*, vol. 1, pp. 76–83, 2005.

[27] T. Sudo, T. Yosijoka, K. Suzuki, and S. Yamazaki, "Method of Manufacturing Granulated Silica Powder, Method of Manufacturing Vitreous Silica Crucible," in *European Patent Office*, 2012.

[28] M. Wünscher, A. Lüdge, and H. Riemann, "Growth Angle and Melt Meniscus of the RF-heated Floating Zone in Silicon Crystal Growth," *Journal of Crystal Growth*, vol. 314, pp. 43–47, 2011.

[29] H. Herzer, W. Hensel, and G. Matuszak, "Method for the Manufacture of Dislocation-free Monocrystalline Silicon Rods," in *Google Patents*, 1988. https://patents.google.com/patent/US4722764A/en.

[30] A. Kravtsov, "Development of Silicon Growth Techniques from Melt with Surface Heating," *IOP Conference Series: Materials Science and Engineering*, vol. 355, no. 1, 2018.

[31] A. Kravtsov, "The Method of Growing Silicon Crystals and Device for its Implementation," in *Google Patents*, 2018. https://patents.google.com/patent/LV15452A/en.

[32] A. Kravtsov, K. Surovovs, and J. Virbulis, "Float Zone Single Crystals for Testing Rods, Pulled under Electron Beam Heating," in *IOP Conference Series: Materials Science and Engineering*, vol. 503, 2019.

[33] H. Riemann, N. Abrosimov, and N. Noetzel, "Doping of Silicon Crystals with Bi and other Volatile Elements by the Pedestal Growth Technique," *ECS Transactions of the Electrochemical Society*, vol. 3, no. 4, pp. 53–59, 2006.

[34] A. Kravtsov and G. Chikvaidze, "Experimental Verification of the Contamination Reduction of Silicon During Electron Beam Melting due to the Use of a Gas-dynamic Window," *IOP Conf. Series: Materials Science and Engineering*, vol. 1100, no. 1, p. 012037, 2021.

[35] Silicon metallurgy company, "KEPP EU." http://keppeu.lv/en/.

[36] A. Kravtsov, A. Shagun, and A. Kravtsov, "New Feedstock for C-Si Photovoltaics," in *IOP Conference Series: Materials Science and Engineering*, vol. 77, 2015.

[37] C.-W. Lan, C.-K. Hsieh, and W.-C. Hsu, *Czochralski Silicon Crystal Growth for Photovoltaic Applications*, pp. 25–39. Berlin, Heidelberg: Springer Berlin Heidelberg, 2009.

[38] A. Krauze, J. Virbulis, and A. Kravtsov, "Modeling Electron Beam Parameters and Plasma Interface Position in an Anode Plasma Electron Gun With Hydrogen Atmosphere," *IOP Conference Series: Materials Science and Engineering*, vol. 355, no. 1, 2018.

[39] W. C. Dash, "Growth of Silicon Crystals Free from Dislocations," *Journal of Applied Physics*, vol. 30, pp. 459–474, 1959.

[40] W. C. Dash, "Improvements on the Pedestal Method of Growing Silicon and Germanium Crystals," *Journal of Applied Physics*, vol. 31, no. 4, pp. 736–737, 1960.

[41] K. Kim, "Microdefects in Small-diameter Silicon Crystals Grown by the Pedestal Technique," *Journal of Applied Physics*, vol. 50, no. 1, p. 1135, 1979.

[42] R. Gereth, "Growth of Silicon Bicrystals by the Dash Pedestal-Method," *Journal of the Electrochemical Society*, vol. 109, no. 11, p. 1068, 1962.

[43] W. Zulehner, "Historical Overview of Silicon Crystal Pulling Development," *Materials Science and Engineering B: Solid-State Materials for Advanced Technology*, vol. 73, no. 1, pp. 7–15, 2000.

[44] T. Ciszek and T. Wang, "Growth and Properties of Silicon Filaments for Photovoltaic Applications," in *Conference Record of the Twenty Sixth IEEE Photovoltaic Specialists Conference*, 1997.

[45] W. von Ammon, Y. Gelfgat, L. Gorbunov, A. Mühlbauer, A. Muižnieks, Y. Makarov, J. Virbulis, and G. Müller, "Application of Magnetic Fields in Industrial Growth of Silicon Single Crystals," in *Proceedings of the 6th PAMIR Conference on Fundamental and Applied MHD*, vol. 42, pp. 427–444, 2006.

[46] T. Ciszek, "Growth Of 40 mm Diameter Silicon Crystals By a Pedestal Technique Using Electron Beam Heating," *Journal of Crystal Growth*, vol. 12, pp. 281–287, 1972.

[47] W. Zulehner and D. Huber, "Czochralski-Grown Silicon," in *Crystals* (H. C. Freyhardt, ed.), ch. 2, p. 3, Springer-Verlag, 1982.

[48] S. Coriell and M. Cordes, "Theory of Molten Zone Shape and Stability," *Journal of Crystal Growth*, vol. 42, pp. 466–472, 1977.

[49] C. E. Chang, "Computer Simulation of Convection in Floating Zone Melting: I. Pure Rotation Driven Flows," *Journal of Crystal Growth*, vol. 44, no. 2, pp. 168–177, 1978.

[50] N. Kobayashi, "Computer Simulation of the Steady Flow in a Cylindrical Floating Zone Under Low Gravity," *Journal of Crystal Growth*, vol. 66, no. 1, pp. 63–72, 1984.

[51] A. Mühlbauer, W. Erdmann, and W. Keller, "Electrodynamic Convection in Silicon Floating Zones," *Journal of Crystal Growth*, vol. 64, no. 3, pp. 529–545, 1983.

[52] A. Mühlbauer, A. Muiznieks, J. Virbulis, A. Lüdge, and H. Riemann, "Interface shape, heat transfer and fluid flow in the floating zone growth of large silicon crystals with the needle-eye technique," *Journal of Crystal Growth*, vol. 151, no. 1, pp. 66–79, 1995.

[53] A. Muhlbauer, A. Muiznieks, and H.-J. Lessmann, "The Calculation of 3D High-Frequency Electromagnetic Fields During Induction Heating Using the BEM," *IEEE Transactions on Magnetics*, vol. 29, no. 2, pp. 1566–1569, 1993.

[54] G. Ratnieks, A. Muiznieks, L. Buligins, G. Raming, A. Mühlbauer, A. Lüdge, and H. Riemann, "Influence of the Three Dimensionality of the HF Electromagnetic Field on Resistivity Variations in Si Single Crystals During FZ Growth," *Journal of Crystal Growth*, vol. 216, no. 1, pp. 204–219, 2000.

[55] R. Menzel, H. Riemann, and N. Abrosimov, "Numerical Model for Si Single Crystal Growth From Melt in a Si Granular Bed," in *Modelling for Electromagnetic Processing*, pp. 465–469, 2014.

[56] K. Dadzis, R. Menzel, M. Ziem, T. Turschner, H. Riemann, and N. Abrosimov, "High-frequency Heat Induction Modeling for a Novel Silicon Crystal Growth Method," in *Modelling for Materials Processing*, pp. 31–36, 2017.

[57] K. Dadzis, R. Menzel, H. Riemann, and N. Abrosimov, "Development of the Granulate Crucible Method for Growth of Large Silicon Crystals," in *Proceedings of CSSC-10*, 2018.

[58] M. Lorenz-Meyer, R. Menzel, K. Dadzis, A. Nikiforova, and H. Riemann, "Lumped Parameter Model for Silicon Crystal Growth from Granulate Crucible," *Crystal Research and Technology*, vol. 55, p. 2000044, 2020.

[59] FEMAG S.A., Belgium, "FEMAG/FZ software." https://www.femagsoft.com/ products/femag-fz.html, retrieved January 30, 2022.

[60] M. Andreeta and A. Hernandes, "Laser-Heated Pedestal Growth of Oxide Fibers," in *Springer Handbook of Crystal Growth* (G. Dhanaraj, K. Byrappa, V. V. Prasad, and M. Dudley, eds.), ch. 13, pp. 393–419, Springer-Verlag, 2010.

[61] M. Wunscher, A. Ludge, and H. Riemann, "Crucible-free Pulling of Germanium Crystals," *Journal of Crystal Growth*, vol. 318, pp. 1039–1042, 2011.

[62] G. Ratnieks, A. Muižnieks, and A. Mühlbauer, "Modelling of Phase Boundaries for Large Industrial FZ Silicon Crystal Growth with the Needle-eye Technique," *Journal of Crystal Growth*, vol. 255, pp. 227–240, 2003.

[63] K. Lācis, *3D Mathematical Modeling of Influence of Magnetic Fields on Melt Flow in Floating Zone Crystal Growth Process*. PhD thesis, University of Latvia, Riga, Latvia, 2010.

[64] P. Dular and C. Geuzaine, "A general environment for the treatment of discrete problems." http://getdp.info/.

[65] S. Fan, G. Plascencia, and T. Utigard, "High Temperature Electric Conductivity of Pure Silicon," *Canadian Metallurgical Quarterly*, vol. 47, no. 4, pp. 509–512, 2008.

[66] W. Keller and A. Mühlbauer, *Floating-Zone Silicon.* Marcel Dekker, Inc., 1981.

[67] D. Meeker, "MathFEMM – The Mathematica Interface to FEMM 4.2." https://www.femm.info/Archives/doc/mathfemm.pdf.

[68] G. Ratnieks, A. Muižnieks, A. Mühlbauer, and G. Raming, "Numerical 3D Study of FZ Growth: Dependence on Growth Parameters and Melt Instability," *Journal of Crystal Growth*, vol. 230, pp. 48–56, 2001.

[69] J. Virbulis, *Numerische Simulation der Phasengrenzen und Schmelzenstromung bei der Züchtung von Siliziumeinkristallen mit dem Floating-Zone Verfahren.* PhD thesis, University of Latvia, Riga, Latvia, 1997.

Acknowledgements

The greatest acknowledgement belongs to my supervisor Jānis Virbulis, who was leading and helping during all stages of the creation of this thesis. I am grateful for the opportunities to work in the ERDF projects, for guiding software development, for publication opportunities, for valuable suggestions and corrections. A number of the used analytical estimations is heavily based on his experience and previous work. This work would not be possible without his help and supervision.

I would also like to thank Andrejs Sabanskis, Armands Krauze and Matīss Plāte for supplementing the main modelling software, which was originally intended for floating zone method, with the code necessary for the modelling of the pedestal method. I am also grateful to Andrejs and Matīss for answers to my questions and other help during the creation of the thesis. I thank all colleagues from the Laboratory of Semiconductor Technologies of the Institute of Numerical Modelling, as well: Dagis Daniels Vidulejs, Maksims Surovovs, Valts Liepiņš, Krišjānis Kalme, Kristers Kokars. I express gratitude to Anatoly Kravcov from the KEPP EU company for performing the experiments of crystal growth from pedestal and for cooperation during the work in ERDF projects and during the preparation of scientific publications.

For the financial support during the work on this thesis, I thank the following project: "LU doktorantūras kapacitātes stiprināšana jaunā doktorantūras modeļa ietvarā" – Latvijas Universitāte, Līguma Nr. 8.2.2.0/20/I/006.

I am deeply thankful to Vika for love and support.